STUDY OF THE VALENCE TAUTOMER COMPLEX [CO(SQ)(CAT)(3-TPP)$_2$] FOR APPLICATIONS IN MOLECULAR SPINTRONICS

by

Jared Phillips

A Dissertation

Submitted to the Faculty of Purdue University

In Partial Fulfillment of the Requirements for the degree of

Doctor of Philosophy

Department of Physics at IUPUI

Indianapolis, Indiana

December 2023

THE PURDUE UNIVERSITY GRADUATE SCHOOL

STATEMENT OF COMMITTEE APPROVAL

Dr. Ruihua Cheng, Chair

Department of Physics

Dr. Andrew Gavrin

Department of Physics

Dr. Yogesh Joglekar

Department of Physics

Dr. Babak Anasori

Mechanical and Energy Engineering

Dr. Gregory Kenning

Indiana University of Pennsylvania

Approved by:

Dr. Horia Petrache

To Mom and Dad

ACKNOWLEDGMENTS

Special thanks to:

My advisor, Dr. Ruihua Cheng

All the members of my graduate committee

The entire IUPUI Physics Department, past and present

My Grandmother, Ida

My brother

Hermes, the dog

Smithton, Pennsylvania

The obscene amount of time spent playing video games with Jeremy

All my friends and especially my enemies

The artists, outcasts, and madmen who continue to watch over me from the beyond

(Chopin and his handful of Polish soil)

TABLE OF CONTENTS

LIST OF FIGURES

ABSTRACT

Molecular materials exhibiting bistability between two states are intriguing candidates for next generation electronic devices. Two similar classes of materials, known as spin crossover (SCO) and valence tautomers (VT) respectively, are of particular interest due to their multifunctional properties, which are controllable via several external parameters, such as temperature, light irradiation, pressure, magnetic field, and electric field. In recent years, considerable research has been dedicated to better understanding the underlying principles that govern the behavior of these materials, so that their implementation into nano-based devices might be achieved.

In this report, a systematic study of the valence tautomer molecule [Co(sq)(cat)(3-tpp)$_2$] is presented. In the first chapter, the phenomenon of valence tautomerism (VT) occurring in coordination compounds is introduced and described from the perspective of Crystal Field Theory (CFT). Further, the molecular structure and physical properties of the [Co(sq)(cat)(3-tpp)$_2$] molecule are explored. The properties of the ferroelectric material Polyvinylidene fluoride-hexafluoropropylene (PVDF-HFP), and the 2-D Mxene Ti_3C_2 are also discussed.

The next section details equipment development and experimental methods. Thin films of VT molecules were prepared from solution via a drop-casting approach. For thin film analysis, we have developed a custom made, fully automated Vibrating Sample Magnetometer (VSM) with a sensitivity on the order of 1×10^{-5} emu, as well as a fully automated, variable temperature, under vacuum electron transport stage, and a magneto-optic Kerr effect apparatus (MOKE). Additional experimental methods used to characterize the VT thin films include X-ray Absorption Spectroscopy (XAS), UV-visible Spectrometry (UV-Vis) and Differential Scanning Calorimetry. Experimental results obtained from these techniques are discussed and analyzed in the third section. PVDF-HFP polarization dependent isothermal spin state switching of [Co(sq)(cat)(3-tpp)$_2$] is also discussed as well as the effects of doping [Co(sq)(cat)(3-tpp)$_2$] with Ti_3C_2, followed by a conclusion and an outline of future work.

CHAPTER 1. INTRODUCTION AND THEORY

1.1 Spin Crossover and Valence Tautomerism

Interest in spin crossover (SCO) molecules has increased in recent years, due to their potential applications in novel electronic devices. Since the first SCO molecule was discovered in 1964, countless more have been synthesized [1-4]. A SCO molecule is a coordination complex consisting of a transition metal ion surrounded by ligands in an octahedral or tetrahedral symmetry [5-7].

The ligands and central ion interact in such a way that the normally degenerate 3d orbitals of the transition metal split into two energy levels, known as the t_{2g} and e_g orbitals. Depending on the strength of the ligand field, the electronic configuration will either adopt what is called a low spin (LS) state or a high spin (HS) state. SCO molecules are bistable, meaning they can inhabit either the LS or HS state and can be controlled by means of some external stimulus. The physical properties possessed by a SCO compound are determined by which state it inhabits and can vary dramatically between the two. Characteristics such as volume, conductivity, color, and magnetic moment all vastly differ between these two states, making these materials interesting prospects for molecular-based devices.

A functionally similar class of molecules known as Valence Tautomers (VT) also consist of a central metal ion surrounded by ligands. A tautomer refers to two structurally identical isomers which a molecule can interconvert between. Essentially, only the location of some of the bonds change in a VT. Like SCO materials, cobalt dioxelene VTs exhibit a bistability between a LS (d^6 Co^{III}) and HS (d^7 Co^{II}) due to energy splitting of 3d orbitals.

The spin transition of these materials involves an intramolecular exchange of electrons between the core metal ion and redox active ligands [8-11]. The mechanisms for altering the spin states of VTs are the same as those of SCOs. In a typical cobalt ion valence tautomer complex, the valence transition is LS-Co^{III} (SQ)(Cat)L $\leftrightarrow$ HS-Co^{II}(SQ)(SQ)L, where SQ is the *o*-semiquinonate, and Cat is the *o*-cathecholate form of the redox active dioxelene molecule, and L is a redox innocent diamine ligand [9]. The electron transfer from LS to HS consists of the reduction of the Co^{III} to Co^{II} by a Cat. Conversely, when going from HS to LS, the SQ oxidizes the Co^{II} form of the central ion. In the LS to HS process, the Cat is oxidized into a SQ, and in the HS to LS process the SQ is reduced to a Cat (Fig 1.1).

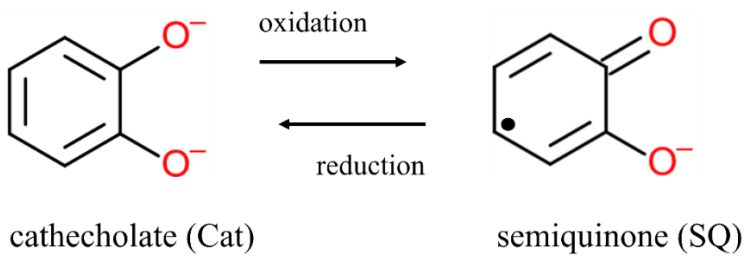

Figure 1.1 The semiquinone and cathecholate forms of the o-quinone molecule.

The unique properties of valence tautomers arise both due to low orbital mixing between the metal center and the ligands, which essentially causes the molecule to adopt a localized charge distribution, and because the energy difference between the two isomers is small [10]. These conditions allow for the characteristic intramolecular charge transfer of VT complexes.

1.2 Molecular Structure and Properties of [Co(sq)(cat)(3-tpp)$_2$]

The valence tautomer molecule, [Co(sq)(cat)(3-tpp)$_2$], consists of a central cobalt ion bonded to a SQ and Cat ligand (both $C_6H_4O_2$) and two 3-thienlpyridine ligands (C_9H_7NS) with a full chemical formula of $C_{46}H_{55}CoN_2O_4S_2$ (Figure 1.2), and with a length in the vertical direction of roughly 17 Å. As this is a newly synthesized molecule, efforts to characterize its unique properties are ongoing, however, initial experiments conducted by our research group show that it shares many traits with other valence tautomers. Like other VT molecules, [Co(sq)(cat)(3-tpp)$_2$] appears to display a distinct transition temperature, $T_{1/2}$. This temperature refers to the point where a VT molecule has an equal portion of molecules in the LS and HS state. The rate at which a VT molecule switches from LS to HS and vice versa, as a function of temperature, is generally molecule specific, and often displays hysteresis-like behavior. Another trait of [Co(sq)(cat)(3-tpp)$_2$] reminiscent of other VT molecules is its high degree of photoactivity, which will be discussed further in Chapter 3.

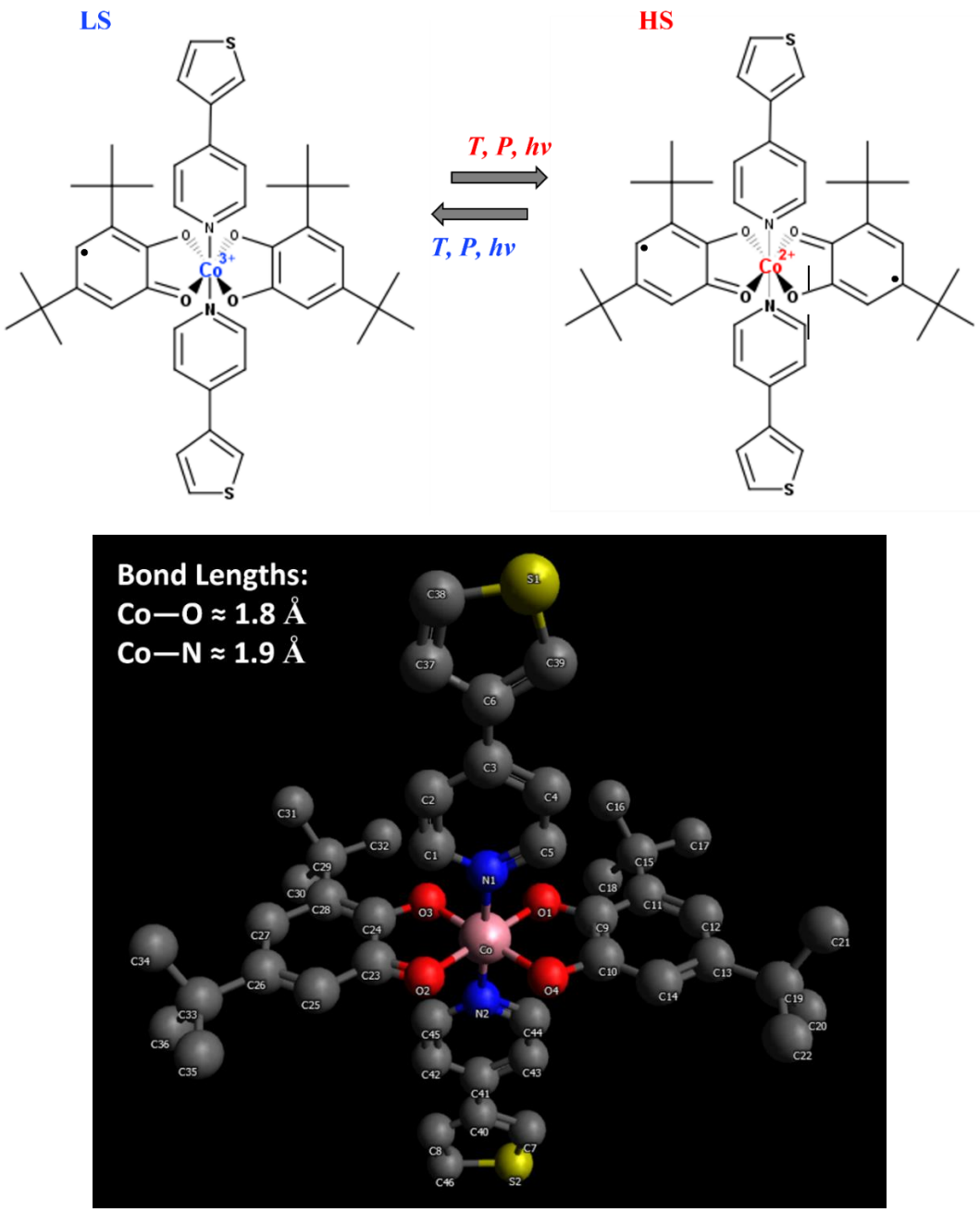

Figure 1.2 (Top) The LS and HS forms of [Co(sq)(cat)(3-tpp)$_2$]. 3-D ball-and-stick image of [Co(sq)(cat)(3-tpp)$_2$]

1.2.1 Thermodynamic Properties of [Co(sq)(cat)(3-tpp)2]

The interconversion between LS-Co^{III} and HS-Co^{II} is an entropy-driven process. The entropy gain in transitioning from LS to HS is due to both a gain in electronic entropy because of the higher spin state degeneracy of the HS spin form and from the higher density of vibrational states of the HS form caused by a lengthening of the bonds between the ligands and central Co ion [Figure 1.3] [12].

The relation between the LS and HS thermal population is given by the Gibbs free energy relation

$$\Delta G = \Delta G_{HS} - \Delta G_{LS} = \Delta H - T\Delta S$$

At low temperatures, the $T\Delta S$ term is small compared to ΔH. When $\Delta H > kT$, only the LS state is populated. As temperature increases, the HS state is more favorable. At a critical temperature, typically denoted, $T_{1/2}$ where $\Delta G = \Delta G_{HS} - \Delta G_{LS} = 0$, there is an equal population of LS and HS molecules with

$$T_{1/2} = \frac{\Delta H}{\Delta S}$$

Further increases to the temperature beyond this point will flip the sign of ΔG.

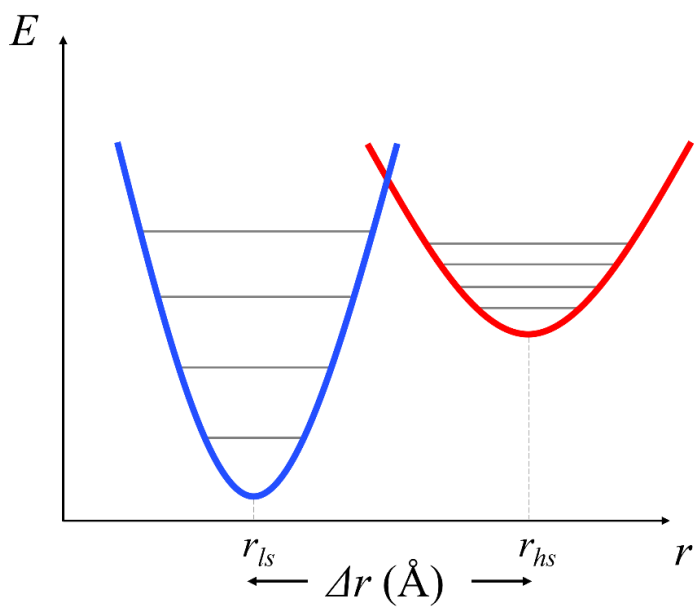

Figure 1.3 Schematic depiction of the potential energy curves of a valence tautomer complex.

1.3 Crystal Field Theory

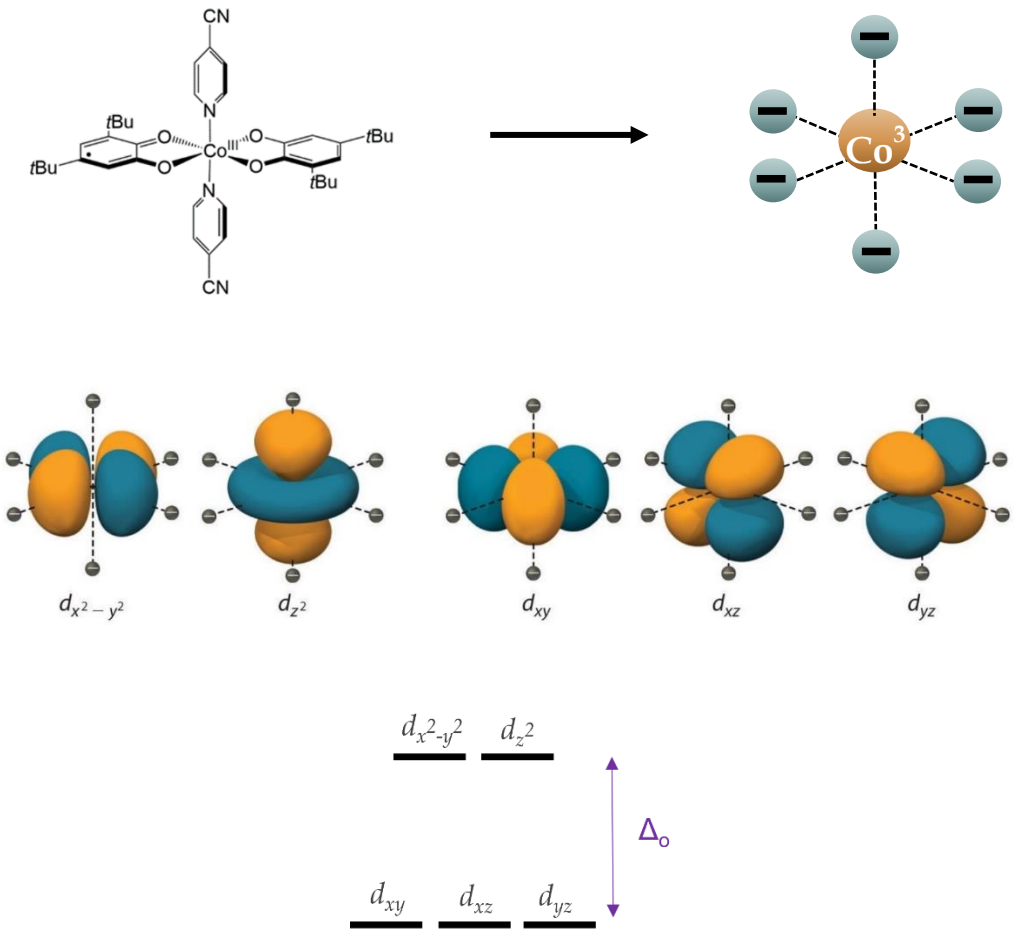

Figure 1.4 Figure 1.4. (a) A Co^{III} complex as described by Crystal Field Theory. The gray spheres represent negative point charges. (b) The interaction with the "point charges" is greater for $d_{x^2-y^2}$ and d_{z^2} since the charges approach directly toward the lobes. The interaction is less for d_{xy} , d_{xz} and d_{yz} since the charges approach in between the lobes. (c) This causes the 3d orbitals of the complex to split.

Crystal Field Theory (CFT) is an analytical approach developed by Hans Bethe in the 1930s [13,14] which describes the breaking of the degeneracy of 3d orbitals due to the interaction between ligands and central transition metal ions. A more precise picture of the energy splitting, and the exact nature of the bonds is described by the later developed Ligand Field Theory, which combines the concepts of CFT and Molecular Bonding Theory [15,16]. CFT is still illuminating however and provides a highly accurate mathematical description of 3d orbital splitting.

CFT takes an electrostatic approach and treats the ligands surrounding the central ion as negative point charges that generate a negative field around the central ion (Figure 1.4a). As the point charges (ligands) approach the metal, the interaction is greater for some due to the octahedral geometry and the shape of the d orbitals (Figure 1.4b). This causes the 3d orbitals to lift their degeneracy and split into two levels, separated by what is known as the crystal field splitting energy, Δ_o (Figure 1.4c). The subscript "o" refers to octahedral splitting.

To construct a model that describes the interaction of the ligands with the central ion, leading to the characteristic breaking of the 3d orbital degeneracy we first consider a hydrogen-like Hamiltonian for the 3d orbitals of the form

$$H_0 = -\left(\frac{\hbar^2}{2m}\right)\nabla^2 - \frac{Ze^2}{r}$$

from where we will then treat the ligands as a perturbing potential.

For an octahedral symmetry with 6 ligands, according to CFT, there are then 6-point charges, with an electrostatic potential energy given by

$$V_r = \sum_{1}^{6} Ze^2 \frac{1}{\boldsymbol{r}} \hat{r}$$

Where $\boldsymbol{r}$, are the coordinates of the 6-point charges with respect to the central metal ion, with atomic number, Z.

With the contribution of one ligand, given in spherical form using Legendre polynomials,

$$V_1 = \frac{Ze^2}{a} \sum_{l=0}^{\infty} \left(\frac{r}{a}\right)^l P_l(cos\theta)$$

Expanding to the first 5 terms,

$$V_1 = \frac{Ze^2}{a}\left[1 + \left(\frac{r}{a}\right) P_1(cos\theta) + \left(\frac{r}{a}\right)^2 P_2(cos\theta) + \left(\frac{r}{a}\right)^3 P_3(cos\theta) + \left(\frac{r}{a}\right)^4 P_4(cos\theta)\right]$$

Due to symmetry, each point charge has a pair separated by π. In other words,

$\cos(\theta + \pi) = -\cos(\theta)$. Meaning, if V_2 is the pair of V_1 then,

$$V_1 + V_2 = \frac{2Ze^2}{a}\left[1 + \left(\frac{r}{a}\right)^2 P_2(cos\theta) + \left(\frac{r}{a}\right)^4 P_4(cos\theta)\right]$$

The same holds true for pairs $V_3 + V_4$ and $V_5 + V_6$.

Inserting the Legendre polynomials and remembering $\cos(\theta)$ will have values of either $\left(\frac{x}{r}\right)$, $\left(\frac{y}{r}\right)$ or $\left(\frac{z}{r}\right)$, depending on which axis the pairs align, leads to a total potential,

$$V = 6\frac{Ze^2}{a} + 35\frac{Ze^2}{4a^5}\left(x^4 + y^4 + z^4 - \frac{3}{5}(x^2 + y^2 + z^2)^2\right) = H$$

Single electron wave function solutions to the Schrodinger equation are generally complex, however, the wave functions of 3d orbitals are customarily taken as linear combinations, since appropriate combinations yield the same energy value, but conveniently in the form of a real solution. These wave functions are of the form

$$Y_2^0 = d_{z^2} = \frac{1}{4}\sqrt{\frac{5}{\pi}} \cdot \frac{-x^2 - y^2 + 2z^2}{r^2} = \frac{1}{4}\sqrt{\frac{5}{\pi}} \cdot (3\cos^2\theta - 1)$$

$$Y_2^{-2} = d_{xy} = Y_2^{-2} - Y_2^2 = \frac{1}{2}\sqrt{\frac{15}{\pi}} \cdot \frac{xy}{r^2}$$

$$Y_2^{-1} = d_{yz} = Y_2^{-1} + Y_2^1 = \frac{1}{2}\sqrt{\frac{15}{\pi}} \cdot \frac{yz}{r^2}$$

$$Y_2^1 = d_{yz} = Y_2^{-1} - Y_2^1 = \frac{1}{2}\sqrt{\frac{15}{\pi}} \cdot \frac{zx}{r^2}$$

$$Y_2^2 = d_{x^2-y^2} = Y_2^{-2} + Y_2^2 = \frac{1}{4}\sqrt{\frac{15}{\pi}} \cdot \frac{x^2 - y^2}{r^2}$$

If we convert to spherical coordinates and separate the radial part of the wave function from the angular part,

$$\psi_{nlm} = R_{nl}(r)\Theta_{lm}(\Theta)\varphi_m(\varphi)$$

From first order perturbation theory,

$$\langle\psi|H|\psi\rangle$$

If

$$H = V(r)V(\theta, \varphi)$$

Then

$$\langle\psi|H|\psi\rangle = \langle R_{nl}|V(r)|R_{nl}\rangle\langle lm|V(\theta, \varphi)|lm'\rangle$$

$$= \int_0^\infty R_{nl}(r)V(r)R_{nl}(r)r^2 dr \int_0^\pi \int_0^{2\pi} \Theta_{lm}(\theta)\Phi(\varphi)V(\theta,\varphi)\Theta_{lm'}(\theta)\Phi(\varphi) sin\theta d\theta d\varphi$$

Recalling the form of the potential V, and substituting $V_0 = 6\frac{Ze^2}{a}$ and $D = 35\frac{Ze^2}{4a^5}$

$$H = V = 6\frac{Ze^2}{a} + 35\frac{Ze^2}{4a^5}\left(x^4 + y^4 + z^4 - \frac{3}{5}r^4\right) \rightarrow V_0 + D\left(x^4 + y^4 + z^4 - \frac{3}{5}r^4\right)$$

In spherical form

$$V_0 + D\left(x^4 + y^4 + z^4 - \frac{3}{5}r^4\right) = V_0 + D\left(r^4 \sin^4\theta\,(\sin^4\varphi + \cos^4\varphi) + r^4\cos^4\theta - \frac{3}{5}r^4\right)$$

Since V_0 is spherically symmetric it doesn't participate in the splitting of energy in CFT, and so it is typically dropped from calculations.

First, we determine the angular terms, starting with φ, noting that for $l = 2$, m has 5 values ranging from -2 to 2

$$\langle \Phi_m | Dr^4 \sin^4\theta\,(\sin^4\varphi + \cos^4\varphi) | \Phi_{m'} \rangle = Dr^4 \sin^4\theta \int_0^{2\pi} e^{im\varphi}\,(\sin^4\varphi + \cos^4\varphi) e^{-im'\varphi} d\varphi$$

$$= \frac{1}{8} D(r^4 \sin^4\theta) \int_0^{2\pi} e^{i\varphi(m-m')}\left(e^{-4i\varphi} + e^{4i\varphi} + 6\right)\, d\varphi$$

Evaluating all combinations of m and m' yields

$$\begin{cases} \frac{3\pi}{2} D(r^4 \sin^4\theta) \;\; for\; m = m' \\ \frac{\pi}{4} D(r^4 \sin^4\theta) \;\; for\; m = m' \pm 4 \\ 0\; else \end{cases}$$

The 5x5 determinant will thus consist of 7 non-zero terms

$$\begin{bmatrix} \langle 2|H|2\rangle & 0 & 0 & 0 & \langle 2|H|-2\rangle \\ 0 & \langle 1|H|1\rangle & 0 & 0 & 0 \\ 0 & 0 & \langle 0|H|0\rangle & 0 & 0 \\ 0 & 0 & 0 & \langle -1|H|-1\rangle & 0 \\ \langle -2|H|2\rangle & 0 & 0 & 0 & \langle -2|H|-2\rangle \end{bmatrix} = 0$$

From here, the Hamiltonian becomes difficult to solve practically. However, by using symmetry adapted orbitals derived from Ligand Field theory [15, 16] we can approximate the full energy determinant.

$$\begin{bmatrix} Dq & 0 & 0 & 0 & 5Dq \\ 0 & -4Dq & 0 & 0 & 0 \\ 0 & 0 & 6Dq & 0 & 0 \\ 0 & 0 & 0 & -4Dq & 0 \\ 5Dq & 0 & 0 & 0 & Dq \end{bmatrix} = 0$$

where

$$q = \frac{2}{105}\langle r^4 \rangle = 486{a_0}^4$$

$$\langle r^4 \rangle = \int_0^\infty r^4 r^2 |R_{32}(r)|^2 dr = 2.5 \times 10^4 {a_0}^4$$

and

$$Dq = \frac{Ze^2}{6a^5}\langle r^4 \rangle$$

Finding the energy eigenvalues for the 5 x 5 matrix gives two values

$E(t_{2g}) = -4Dq$ for d_{xy} , d_{yz} , d_{zx}, designated the t_{2g} orbitals

and

$E(e_g) = 6Dq$ for d_{z^2} , $d_{x^2-y^2}$, designated the e_g orbitals.

This result demonstrates the breaking of the degeneracy for the frontier d orbitals in transition metal complexes surrounded by an octahedral ligand field. The energy difference between the two energy equals $10Dq$, by convention, which is equal to the octahedral splitting energy, Δ_o. The total width of Δ_o depends on the strength of the ligand field, but the total difference between t_{2g} and e_g will always equate to $10Dq$.

If we consider a lone Co^{III} ion, the 6 valence electrons will adopt a configuration that creates the least amount of paired electrons (Figure 1.5). However, when the Co^{III} is the central ion in a coordination complex, the way the electrons fill the 3d orbitals depends on which state the molecule inhabits. In the LS, diamagnetic state, the energy gap is larger than the spin pairing energy (the energy required to pair up electrons), and Hund's rule is not followed; all 6 electrons will pair up. When the molecule is in the HS, paramagnetic state, the energy gap is less than the pairing energy, and so the electrons will populate all unfilled orbitals before they begin to pair up.

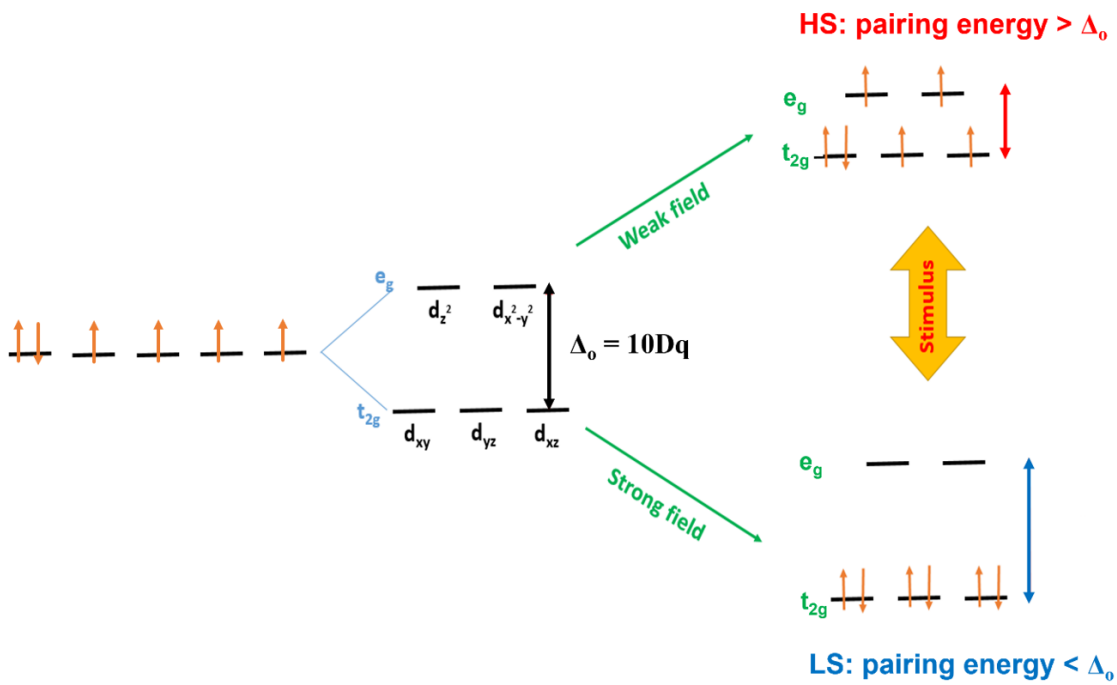

Figure 1.5 (left) The 3d orbital configuration of a lone Co^{III} ion. (middle) The splitting of the 3d orbitals into the t_{2g} and e_g, respectively due to the presence of an octahedral ligand field. (right) The electronic configuration of 3d orbitals in the LS and HS states, respectively.

The colors observed in transition metal complexes are most often due to the wavelengths of light that are transmitted or reflected which are complementary to the colors that are absorbed. [Co(sq)(cat)(3-tpp)$_2$] appears green, so by using the complementary colors of green on the color wheel, we can estimate that the wavelength of light absorbed is in the red range from around 620-800 nm (Figure 1.6). When the molecule absorbs red light it causes d-d transitions from the t_{2g} to e_g orbitals to occur, meaning we can directly approximate the octahedral splitting energy for one molecule by,

$$\nu = \frac{c}{\lambda} = \frac{3 \times 10^8 m/s}{750 \times 10^{-9} m} = 4 \times 10^{14}\ \text{Hz}$$

and,

$$E = h\,\nu = 2.6 \times 10^{-19}\ \text{J} = 1.6\ \text{eV} \approx \Delta_o$$

thus

$$\Delta_o \approx 1.6\ \text{eV} = 156\ \text{kJ/mol}$$

However, it is worth noting that with [Co(sq)(cat)(3-tpp)$_2$] we do not observe a color change upon a change in spin state. This could be due to several factors. For one, the color of the molecule in

solution is rather dull, typical of complexes with weak d-d transition absorption bands. The color change upon spin state switching might simply not be visible to the human eye. This might also be because the molecule does not readily change its spin state due to low cooperativity between the molecules. In the extreme case, the color we observe might not be due to d-d transitions at all. The green we observe might be due to the charge transfer bands between the central metal ion and the attached ligands. The intensity of these absorption bands are significantly more intense than those caused by d-d transitions [17].

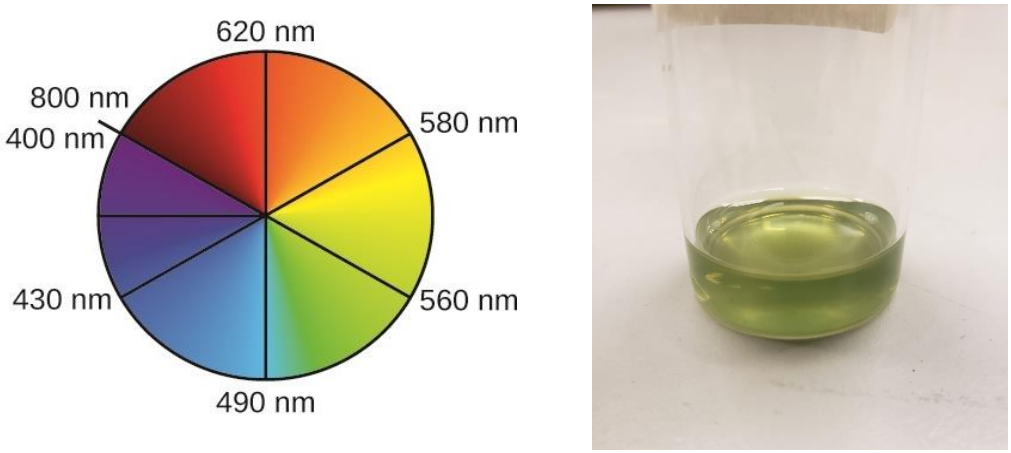

Figure 1.6 (left) In the color wheel, complementary colors are located directly across from each other. (right) A solution of [Co(sq)(cat)(3-tpp)$_2$] dissolved in toluene appears green, meaning it absorbs light in the red range.

1.3 Properties of the Ferroelectric Polyvinylidene fluoride-hexafluoropropylene (PVDF-HFP)

Ferroelectric polymers consist of polymer chains that exhibit ferroelectric behavior, meaning that they can maintain a permanent electric polarization that can be reversed by an electric field. Among ferroelectrics, Polyvinylidene fluoride (PVDF) stands out, due to its compact structure, chemical stability, and large permanent dipole moment [18]. The structure of PVDF consists of repeated chains of -CH_2-CF_2-, which can take on a trans (T) or gauche (G) formation. PVDF is generally polymorphous, consisting of multiple crystalline phases. The three phases of PVDF, are the α-phase (TGTG), the β-phase (TTTT), and the γ-phase (T_3GT_3G). The α-phase is the most thermally stable phase at room temperature, which is electrically inactive due to the orientation of

the fluorine ions effectively cancelling out the dipole moment. The γ-phase is an electrically active phase; however, the effect is very weak due to the T_3GT_3G alignment, and it also requires the polymer to be subjected to temperatures near its melting point. The most useful phase for electronics is the β-phase, where the chains align providing a large dipole moment as well as thermal stability. A high β-phase proportion can be achieved by annealing PVDF at approximately 130 ºC. The addition of the co-polymer Polyvinylidene Fluoride Hexafluoropropylene (PVDF-HFP) also helps increase the β-phase (Figure 1.7) [19-25].

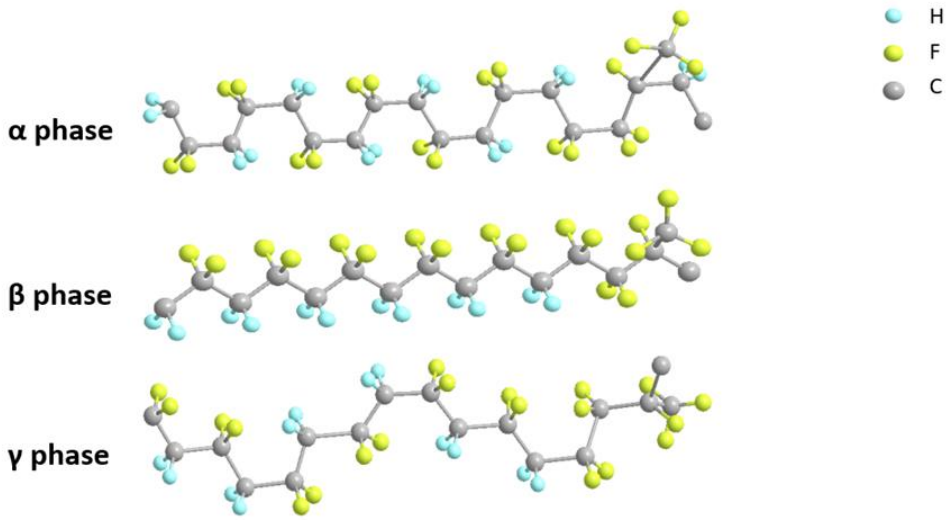

Figure 1.7 Image of PVDF-HFP in α-phase, β-phase and γ-phase

1.4 Structure and Properties of 2-D MXenes

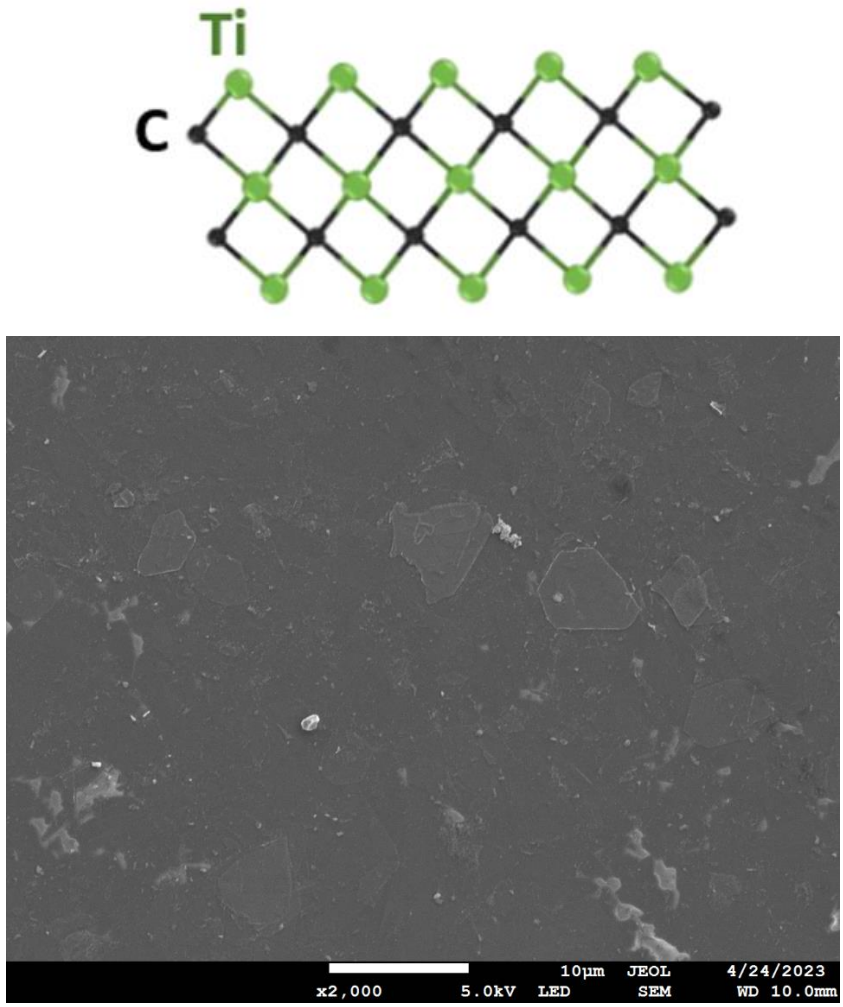

Figure 1.8 (Top) Schematic chemical structure of Ti_3C_2 2D MXene materials. Large green balls represent Ti atoms and small black balls represent C atoms. (Bottom) SEM image of a ~40 nm spin coated thin film of Ti_3C_2

First synthesized in 2011 [26-41], MXenes are a class of two-dimensional (2D) transition metal carbides and nitrides. A 2D flake of MXene, consists of layers of a transition metal (M) interwoven with layers of carbon or nitrogen (X), with a naming convention of $M_{n+1}X_nT_x$ where T_x is a functional group, such as O, F, OH or Cl. Ti_3C_2 was the first MXene to be synthesized and remains one of the most widely studied (Figure 1.8). MXenes possess several interesting properties including the mechanical and electrical properties of transition metal carbides and nitrides and hydrophilic properties due to their functionalized surfaces. The potential applications of MXenes

are numerous and cover a wide range of fields including energy storage, composites, sensors, water purification and metamaterials. Of particular interest in our lab is the potential use of MXenes as a substrate for SCO and VT thin films and as a doping material, both of which will be discussed later.

CHAPTER 2. EQUIPMENT DEVELOPMENT AND EXPERIMENTAL METHODS

2.1 Thin Film Preparation

Synthesis of [Co(SQ)(Cat)(3-tpp)$_2$] (3-tpp = 3-thienylpyridine) thin films was carried out by first layering a solution of [Co^{II}(SQ)$_2$]$_4$ (270 mg, 0.13 mmol) in 8 mL of toluene on top of a solution of 3-tpp (172 mg, 1.07 mmol) in 5 mL of dichloromethane, which formed blue crystals after a few weeks. The crystals were then washed with toluene and dried under vacuum at 100 ºC for 24 hours resulting in a dark powder as described previously [42].

Fabricating thin films of [Co(sq)(cat)(3-tpp)$_2$] was done using a drop casting technique. Drop casting works by first dissolving the powder form of a molecule in a suitable solvent. This solution is then "drop cast" on a chosen substrate. After the solvent fully evaporates, only the solute molecule remains. An illustration of this process can be seen in Figure 2.1.

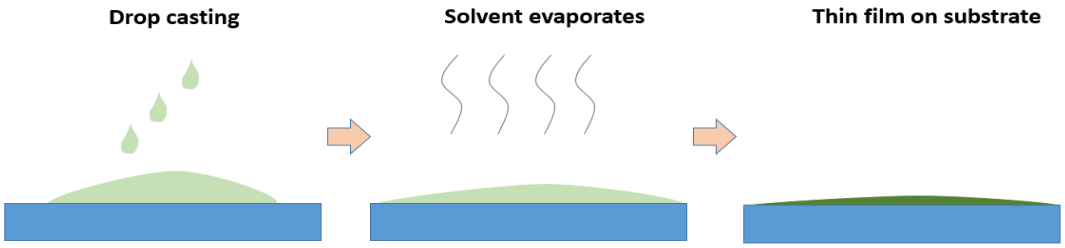

Figure 2.1 The three-step process of drop casting. The solution is first drop cast onto the substrate, after which the solvent begins to dry. Once the solvent is fully dry, only a thin film of the desired molecule remains.

For [Co(sq)(cat)(3-tpp)$_2$] various solvents were tested, including dichloromethane, acetone, methanol and toluene. We found that toluene served as the best solvent, as it led to the best solubility and minimized the "coffee ring" drying effect, which arises due to the surface tension of a droplet tending to push the solute outward as the solvent dries, leading to a crater-like deposition [43]. The approximate thickness of drop cast thin films can be determined by the relation, $t = \frac{V_C}{A}$, where t is the thickness of the film, V_C is the total volume of solute contained in a single drop of solution of volume V_T, and A is the total area fully covered by a drop of solution. For samples used in XAS studies, substrates had surface areas of 1 cm^2, which required a total drop volume,

V_T of 25 µL to fully cover the substrate. Using a solute to solvent volume ratio of 0.0009 mL of [Co(sq)(cat)(3-tpp)$_2$] powder (ρ = 1100 kg/m^3) to 3 mL of toluene (ρ = 867 kg/m^3), a single drop, containing a V_C = 1.5 × 10^{-6} mL, created a thin film of [Co(sq)(cat)(3-tpp)$_2$] with a nominal thickness of 75 nm. For the creation of electron transport study samples, the deposition surface was roughly 0.5 cm^2 and each V_T = 5 µL drop resulted in a roughly 30 nm thick layer of [Co(sq)(cat)(3-tpp)$_2$]. The sensors used, which will be discussed further in Section 2.3, had electrode heights measuring 200 nm thick, and required roughly 10 individual drops of solution for optimal functionality.

2.2 Development of a Home-made High Sensitivity Vibrating Sample Magnetometer

For measuring the magnetic properties of thin films we developed a custom-built, fully automated and remotely controlled vibrating sample magnetometer (VSM) [44]. A VSM functions based on Faraday's Law, which states that the motion of a magnetized material will generate a voltage in a conductive wire. In the case of a VSM, the sample is oscillated sinusoidally near a pair of pickup coils. For magnetic samples with dimensions much smaller than the pickup coils, the sample can be treated like a miniature magnet generating a magnetic field (Figure 2.2) given by the dipole approximation,

$$B(r) = \frac{\mu_0}{4\pi}\left[\frac{3\boldsymbol{r}(\boldsymbol{m}\cdot\boldsymbol{r})}{r^5} - \frac{\boldsymbol{m}}{r^3}\right]$$

where m is the magnetic moment of the sample.

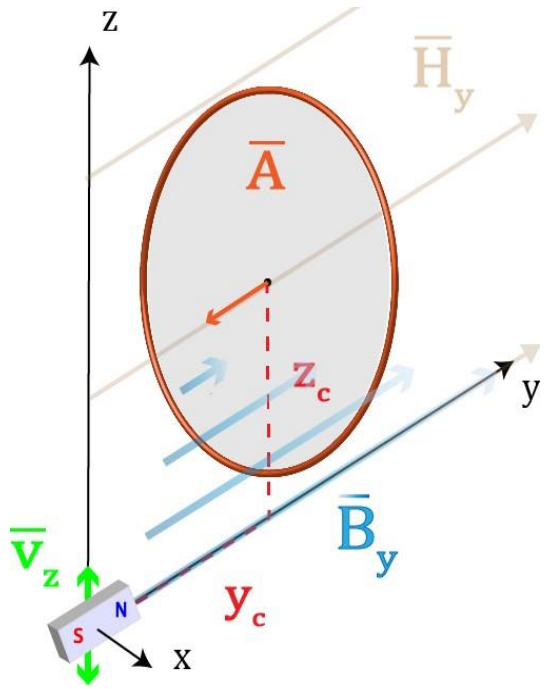

Figure 2.2 y-component of magnetic flux, B_y, for a dipole in a uniform magnetic field, H_y, passing through a single turn of a pickup coil of area, A, centered on the x axis. v_z indicates the direction of oscillation of the dipole [16].

The flux through an individual loop of wire in a pickup coil is

$$\Phi = \int_A B(r) \cdot dA$$

where an induced voltage, $|d\Phi/dt| = |V_{ind}|$ is generated due to the oscillation of a magnetic sample.

An alternative way of representing V_{ind} mathematically that is rather helpful during the design process of a VSM utilizes the theory of reciprocity, which states that the mutual conductance coupling two coils is independent of which one carries the current

$$\frac{\Phi_{21}}{I_1} = \frac{\Phi_{12}}{I_2}$$

Φ_{21} represents the flux through coil 2 due to the field generated by coil 1 and vice versa. If coil 1 is replaced by a dipole with overall moment $m = I_1 dA_1$, the equality can be rewritten. After substituting, the flux through coil 2 (which equates to one turn of the sensor coil), is given by

$$\Phi_{21} = \frac{B_2 m}{I_2}$$

where B_2 is the B-field in the y-direction at the sample due to a fictitious current in the coils, I_2, and m is the magnetic moment of the sample. When the magnetic moment is oscillated in the z direction the V_{ind} is

$$\frac{d\Phi_{21}}{dt} = \frac{d\Phi_{21}}{dz}\frac{dz}{dt} = v_z \frac{d\left(\frac{B_2 m}{I_2}\right)}{dz} = m v_z S(r)$$

This is ultimately the quantity measured by a VSM. Here, v_z is the velocity of the sample in the form of Aωcos(ωt), which is controlled by the user. The $S(r)$ term is known as the sensitivity function and depends on the geometry of the sensor coils and their orientation in space with respect to the sample [45,46]. This is the parameter one seeks to maximize in the design process of the VSM.

The base frame of our VSM was built with 2'×4" wood using glue and brass screws to minimize undesired signals. A 9" diameter speaker is attached to an acrylic sheet, with a hole cut from its center, which is affixed to the top of the wooden frame. Glued to the speaker diaphragm is an acrylic disc with a threaded hole in its center where one end of a 32" fiberglass threaded sample rod is fixed. The entire device rests on top of a large rubber mat which helps to reduce mechanical vibration. On the other end of the rod, a threaded delrin cylinder is attached. The cylinder's function is twofold. It acts as a weight, which in principle helps minimize the lateral motion of the sample rod, in addition, the open end of the cylinder allows for the sample holder to be attached and detached easily, while also allowing for fine adjustments of the sample height with respect to the sensor coils. A schematic diagram of the VSM is shown in Figure 2.3.

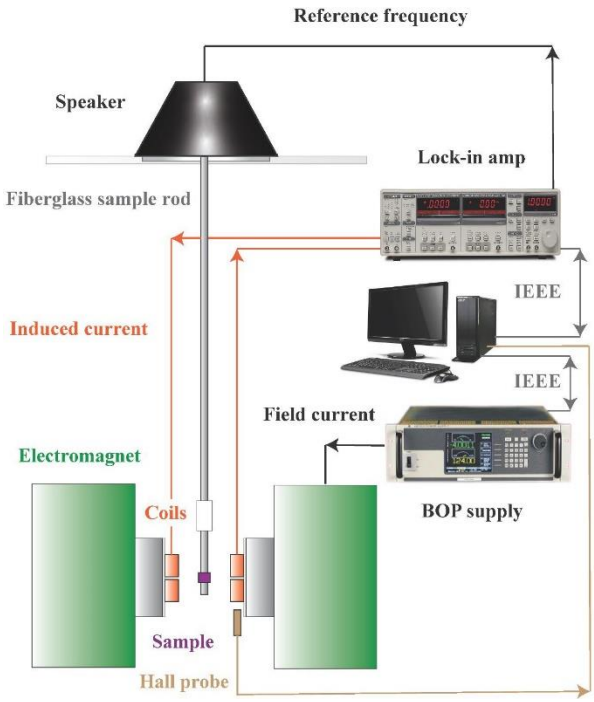

Figure 2.3 A schematic of the constructed VSM. The bipolar power supply (BOP) ramps the magnetizing field, while the lock-in amplifier drives the speaker, with attached sample rod, causing it to oscillate. This creates a time varying flux in the sensor coils, which generates a current. This sinusoidal current is read by the lock-in amplifier and the data are fed into the computer where they are recorded and plotted via LabVIEW.

Each sensor coil consists of approximately 4700 turns of 42 AWG (0.0026" diameter) copper wire wound on a 27.4 outer diameter (OD)/15 inner diameter (ID) mm bobbin. Each pair is separated by 1.2 mm in the z-direction and 20 mm in the y-direction and enclosed within a 3D printed mount pictured in Figure 2.4 (a). The coils are wired together in the Mallinson configuration [47], illustrated in Figure 2.4 (b). The benefits of this configuration are such that the V_{ind} of all four coils add together when the changing flux originates from the space between them (i.e., from the sample). Also, for a changing flux that originates from outside the region between the coils, the undesired emf in the coils is attenuated.

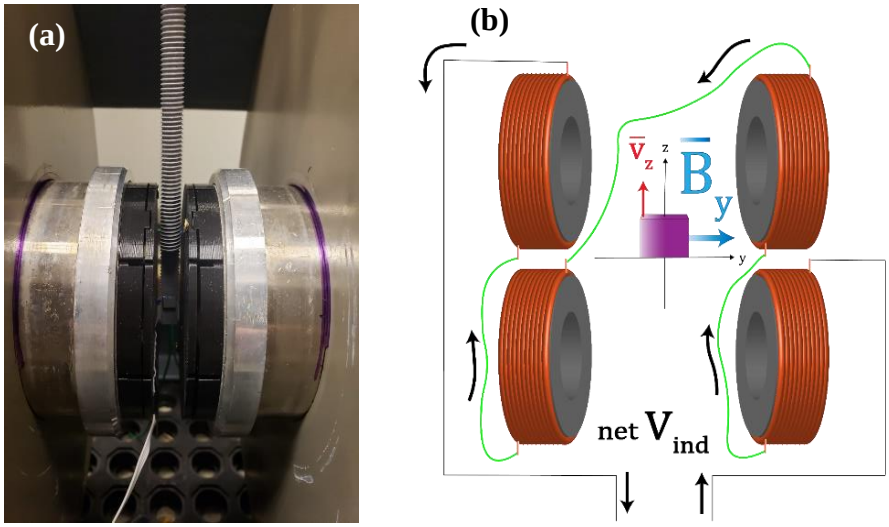

Figure 2.4 (a) A closeup picture of the sample holder and the coils shielded by 3D printed covering. (b) A net V_{ind} is generated in the coils due to the oscillation of the sample in the z direction.

A 1 kW Kepco bipolar power supply (BOP) is used to ramp the field of the electromagnet between ±5000 G, and a Stanford Instruments SR830 lock-in amplifier provides a sinusoidal signal to drive the speaker and reads the output from the sensor coils. To achieve optimal signal output from all four sensor coils, the corresponding values required for the lock-in output voltage (5 V) and frequency (112.91 Hz) were determined experimentally. Additional values determined via experimentation were the minimum required lock-in time constant (1 s) and wait time between data points to allow the lock-in to sufficiently settle (14 s). The BOP and lock-in control are fully automated through a GPIB interface using custom written LabView code.

The VSM was calibrated using two methods. In the first method, a 6 mm diameter, 32 mg nickel disc standard sample from the National Institute of Standards and Technology (NIST) was used to determine the magnetic moment calibration constant. The standard disc has a specific magnetization at a given applied field. In this case, it is 1.753 emu at 5000 Oe. To convert the raw data collected from the lock-in output to units of emu, one finds the ratio of the lock-in value in volts at 5000 Oe with 1.753 emu. Using this method, the conversion constant for the VSM was found to be 4677 emu/V. Additionally, data acquired from the VSM were compared to SQUID data taken for the same thin film samples prepared via sputtering under high vacuum. A VSM hysteresis run of a clean Si substrate, approximately the same dimensions as the thin film substrates, was performed to remove the background from the raw data. This data subtraction step is necessary

because Si substrates, which the thin films were deposited on, are diamagnetic in nature and contribute a negative slope to the overall signal. Following background subtraction, the data were converted to emu units and compared with the SQUID data, which can be seen in Figure 2.5a. Here the magnetic hysteresis data in Figure 2.5b, obtained from SQUID and VSM, show some constraining effects in the low magnetic field region. This is because the sample, prepared under specific conditions, possesses phases other than the desired $Nd_2Fe_{14}B$ phase, and these different phases present antiferromagnetic-like interaction. In the regions where the samples are nearly saturated, at fields greater than ±2500 Oe, the difference between the data acquired by the SQUID and that of the VSM varies between 1.5% and 3%.

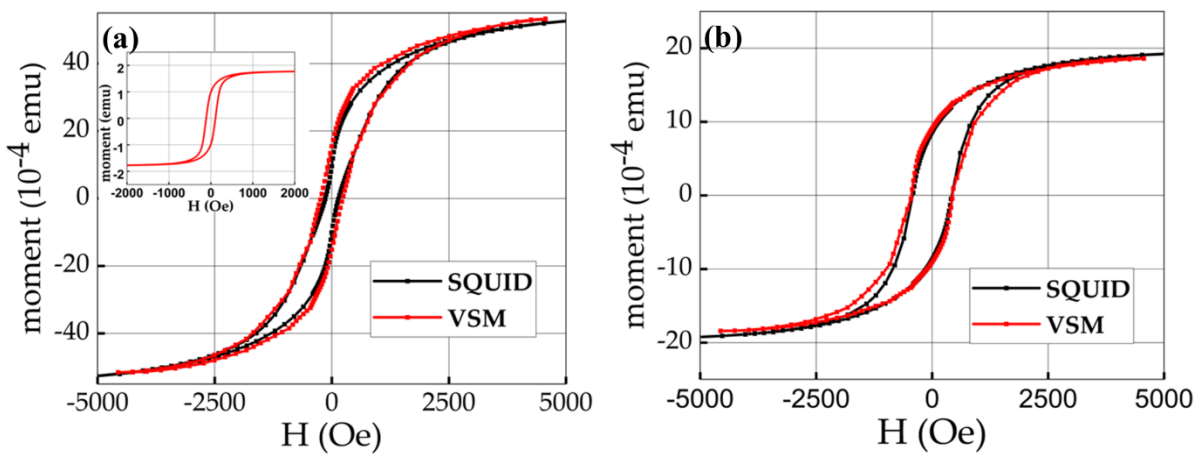

Figure 2.5 (a) and (b) show the comparison of magnetic moment data acquired via a commercial SQUID and the constructed VSM for two separate Nd-Fe-B thin films fabricated under different conditions. The inset of (a) is a hysteresis plot of the Ni disc calibration sample measured by the VSM.

After verifying the calibration of the VSM, 25 nm Fe thin films sputtered on Si substrates were prepared. In plane and out of plane hysteresis measurements were then performed on the thin films. The results, after background subtraction, are shown in Figure 2.6 and are in reasonable agreement with the theoretical values [48]. Approximating the surface area of the measured sample to be 25 mm^2, the total mass of Fe deposited on the substrate would be around 3.1 nanograms. Multiplying this by the reported saturation value of pure Fe, which is equal to 221.71 emu/g, the calculated emu equates to approximately 7×10^{-4} emu. Comparing this theoretical value to the value measured by the VSM results in a percent difference of less than 7% between the two.

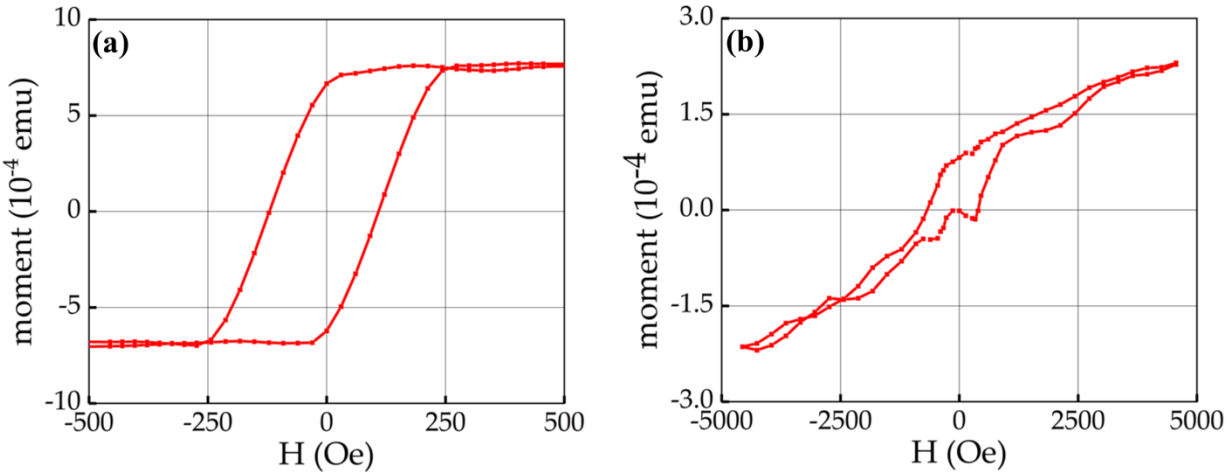

Figure 2.6 Magnetization data of a 25 nm Fe thin film sputtered on a Si substrate. (a) In plane, parallel to the easy axis. (b) Out of plane, perpendicular to the easy axis.

Based on the data, the sensitivity of the VSM is nearly on the order of 1×10^{-5} emu. This is rather promising when considering that there are several potential improvements that can be made to the existing setup. One major factor that likely influences the data is thermal drift caused by the electromagnet, which is currently not water-cooled and becomes noticeably warm. When performing very small signal VSM measurements, as with background subtractions, the data shift slightly with each hysteresis loop iteration.

Room temperature measurements performed on thin films samples of [Co(sq)(cat)(3-tpp)$_2$] provided inconclusive data, likely due to the weak diamagnetic signal of the material being outside the detection limit of the VSM.

2.3 Custom-built Variable Temperature Electronic Transport Device

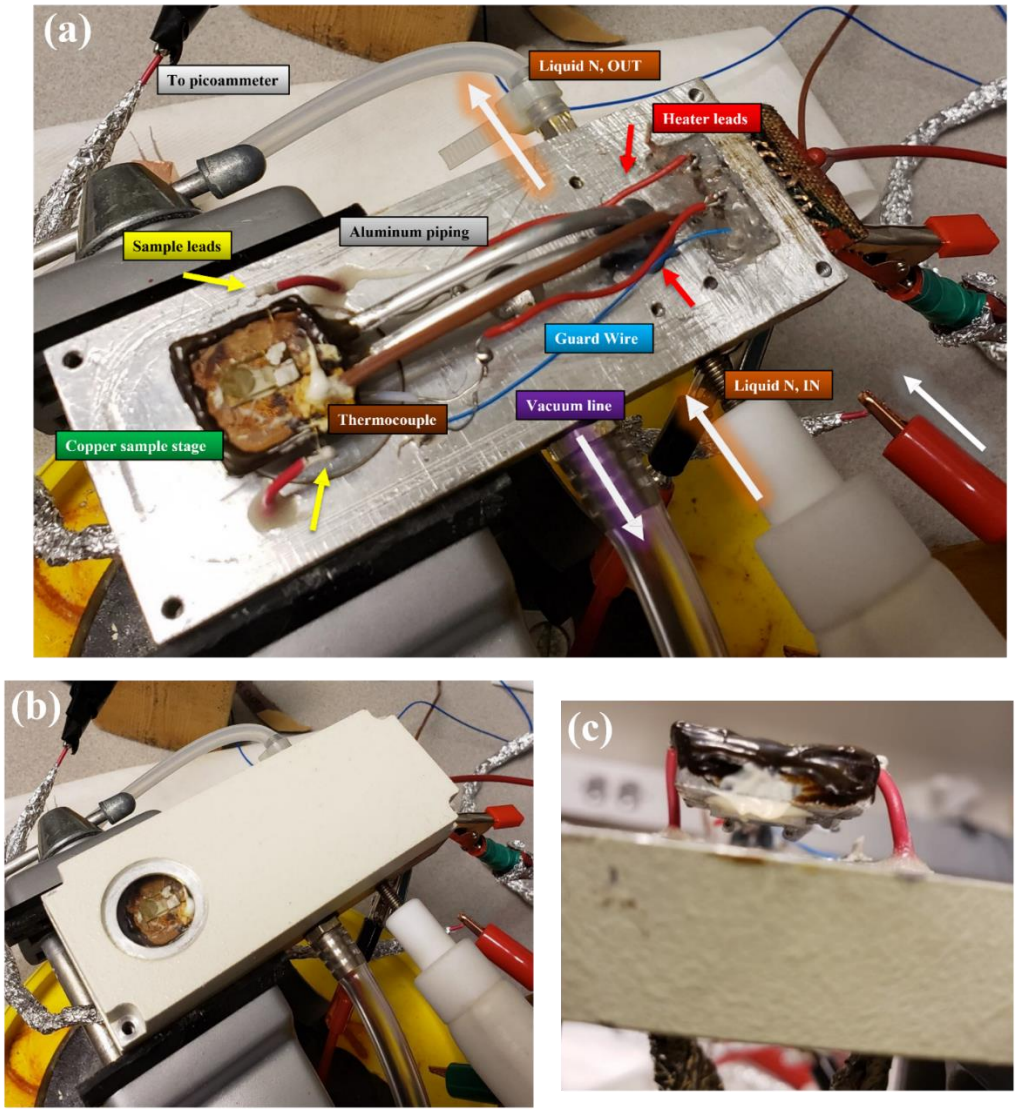

Figure 2.7 (a) A schematic of the custom electronic transport stage. (b) The stage with vacuum viewport cover attached. (c) A closeup profile view of sample stage and heater.

For electron transport experiments, a custom-built stage was constructed. The device is controlled via a fully automated LabVIEW interface, with several custom written programs capable of a variety of variable temperature and bias measurements. Key features include a vacuum sample chamber, a glass viewport for optical studies and a heater combined with a liquid nitrogen

pumping system making the device capable of ramping between temperatures ranging from 80 K – 500 K (Figure 2.7).

The inner sample stage consists of a solid rectangular piece of hollowed-out aluminum capped and sealed by a thin piece of copper, atop which the sample is placed. The hollowed-out area serves as a reservoir for the liquid nitrogen that is pumped through via two connected aluminum tubes. The tubes and sample stage are raised slightly to minimize thermal contact with the rest of the device and to increase energy efficiency. All electronic feedthroughs are sealed with a mix of temperature-resistant epoxy and silicone sealant.

Sample substrates are proprietary interdigitated electrode (IDE) sensors manufactured by MicruX. The electrodes consist of 180 pairs of interdigitated gold electrodes, 5 µm wide with a gap of 5 µm and a height of 200 nm. The underlying glass substrate has dimensions of 10 × 6 × 0.75 mm (Figure 2.8). Solutions of [Co(sq)(cat)(3-tpp)$_2$] were directly drop cast onto the IDE and allowed to fully dry before conducting measurements.

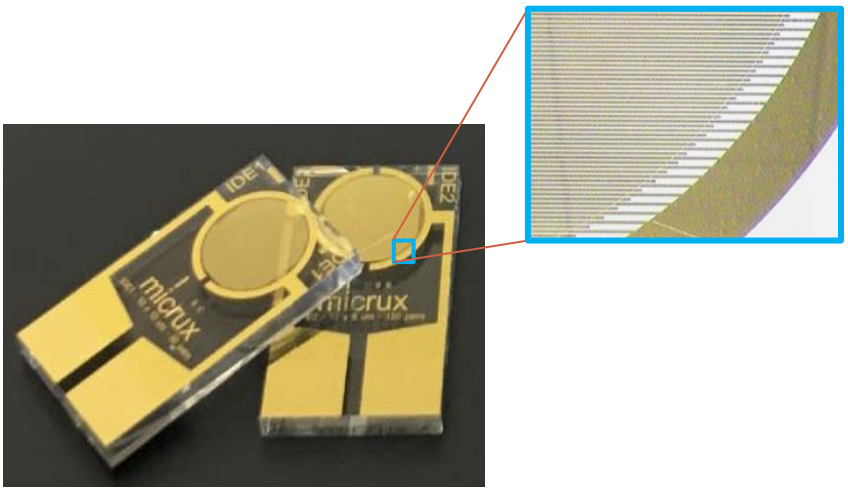

.Figure 2.8 Micrux interdigitated electrodes. Each gold electrode pair measures 200 nm high with a 5 µm gap.

I-V measurements are done using a Keithley 6487 picoammeter interfaced with a PC and controlled by LabVIEW. Samples are connected to the device using high purity gold wires fastened by a DI water-based conductive silver paste. Securing samples to the variable temperature stage is done using Gennel G109 thermally conducting silicone glue.

2.4 X-ray Absorption Spectroscopy (XAS)

XAS is a technique used to investigate the electronic structure of materials. It works by striking atoms with X-rays which causes core electrons to become excited to unoccupied states, or in some cases, to be ejected from the atom entirely [49]. During an XAS measurement, an X-ray beam is ramped over a specified energy range causing excitation of core electrons of the material it passes through. As the energy is increased during a measurement, a sharp peak will appear when a core electron transition energy is reached signifying absorbance. These peaks are known as "edges" and correspond to electrons being excited into unfilled orbitals. These energies correspond to the electron binding energy of the electrons given by the quantum number, *n*; from the Bohr model, K corresponds to *n=1*, L corresponds to *n=2*, etc. Our experiments with cobalt complexes involved the excitation of electrons from core 2p orbitals to unfilled 3d orbitals, thus it is termed L-edge XAS.

From Fermi's golden rule we can approximate the probability of a core electron to absorb a photon, and trigger a transition, which is proportional to the absorption coefficient. First, we consider an electron system with Hamiltonian, H, consisting of two eigenstates, $|\Phi_i\rangle$ (an electron in a core state) and $|\Phi_f\rangle$ (an electron excited to an unoccupied state). We treat the interaction of single photons and electrons as a perturbing, or interacting, Hamiltonian, H_{int}

$$H_{int} \propto \boldsymbol{A}(\boldsymbol{r}) \cdot \boldsymbol{p}$$

where ***A(r)*** is the vector potential of the applied electromagnetic field, in the form of $\hat{\epsilon}e^{-ik\cdot r}$, with $\hat{\epsilon}$ representing the direction of polarization and $\boldsymbol{p}$ is the momentum operator acting on electron states. The $\boldsymbol{A}^2$ term of the vector potential can be ignored in the small energy approximation.
In the general form, the absorption coefficient is proportional to Fermi's golden rule given by

$$\mu(\mathrm{E}) \sim \sum_f \left|\langle \Phi_f | \boldsymbol{A}(\boldsymbol{r}) \cdot \boldsymbol{p} | \Phi_i \rangle\right|^2 \delta(E_f - E_i - \hbar\omega)$$

where E_f and E_i correspond to the energy of the final and initial state and $\hbar\omega$ is equal to the absorbed photon energy, with the entire expression summed over all possible final energy states. The delta function ensures the conservation of energy. A transition will occur only if the final state energy is equal to the initial state energy plus the energy of the absorbed photon.

Typically, the transition probability is reduced to the dipole approximation for single photon-electron transitions, as the wavelength of the incoming radiation is much larger in scale

than the atomic radius of the absorbing atoms ($k \cdot r \ll 1$). This allows for the higher order terms of the vector potential, written as a Taylor expansion, to be ignored so that it can be simplified to

$$\boldsymbol{A}(\boldsymbol{r}) \propto \hat{\epsilon} e^{-ik\cdot r} = \hat{\epsilon}\left[1 - (ik \cdot r) + \frac{1}{2}\,(ik \cdot r)^2 - \cdots\right] \sim \hat{\epsilon}$$

The transition matrix element now becomes

$$\hat{\epsilon}\langle \Phi_f | \boldsymbol{p} | \Phi_i \rangle$$

The momentum form of the matrix element can be changed to position form utilizing the commutator relation,

$$[\boldsymbol{r}, \boldsymbol{H}] = \frac{i\hbar \boldsymbol{p}}{m_e}$$

Leading to

$$\hat{\epsilon}\langle \Phi_f | \boldsymbol{p} | \Phi_i \rangle = -\frac{i m_e}{\hbar}\hat{\epsilon}\langle \Phi_f | [\boldsymbol{r}, \boldsymbol{H}] | \Phi_i \rangle = i m_e \omega_{fi}\, \hat{\epsilon}\langle \Phi_f | \boldsymbol{r} | \Phi_i \rangle$$

Finally, the transition probability, W_{fi}, of a single core electron to an unoccupied state as the result of an absorption of a photon can be approximated as

$$W_{fi} \propto \left|\hat{\epsilon}\langle \Phi_i | \boldsymbol{r} | \Phi_f \rangle\right|^2 \delta(E_f - E_i - \hbar\omega) = M^2 \delta(E_f - E_i - \hbar\omega)$$

The delta function essentially represents the density of unoccupied states, ρ, meaning that the experimentally observed absorption intensity, I_{XAS}, is roughly equivalent to

$$I_{XAS} \sim M^2 \rho$$

Selection rules restrict the types of transitions that may occur due to the symmetry requirement of the wave functions. $\langle \Phi_f | \boldsymbol{r} | \Phi_i \rangle = 0$, unless the change in orbital angular momentum satisfies $\Delta l = \pm 1$. This allows only transitions of the type, $s \to p,\ p \to s,\ p \to d,\ d \to f, etc.$ Theoretically forbidden transitions are still physically possible, although they occur with far less probability.

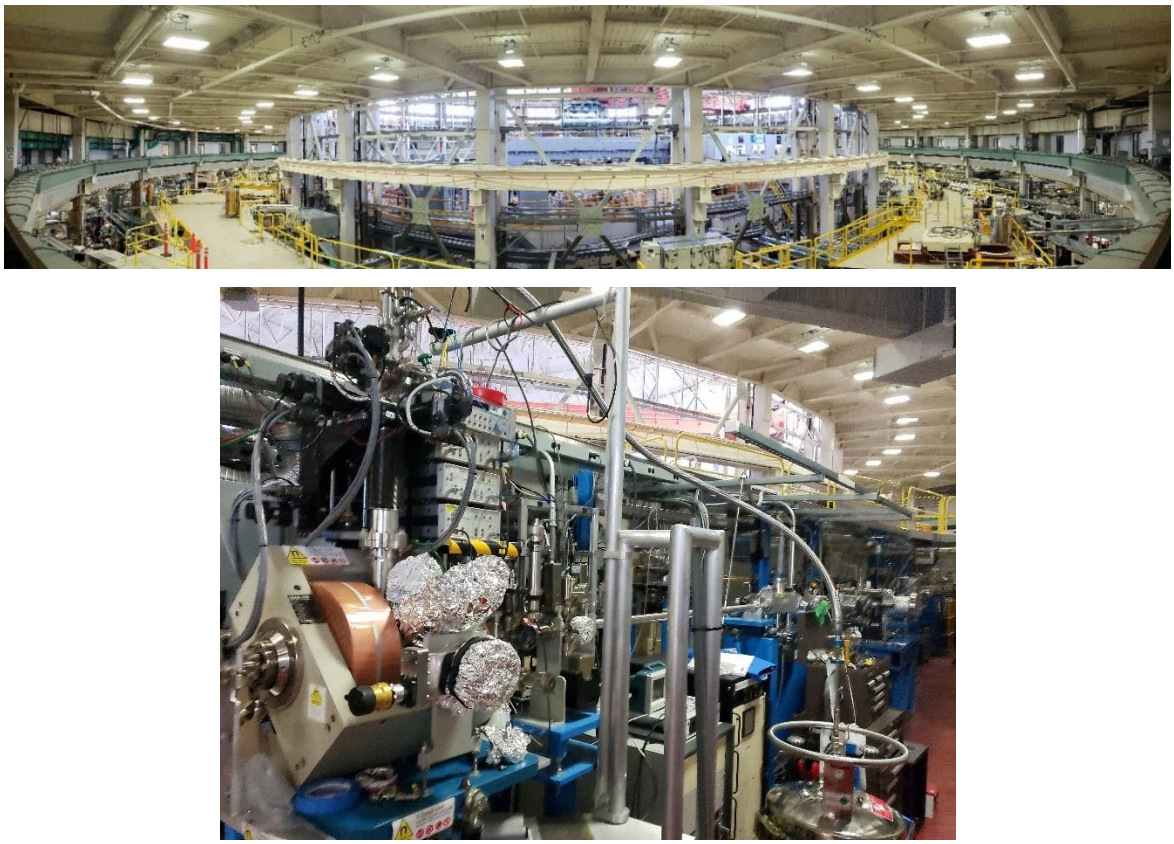

Figure 2.9 Top: View of the ALS facility electron storage ring and individual research stations. Bottom: The 6.3.1.1 beamline (right) and experiment chamber (left).

X-ray absorption experiments were conducted at the Advanced Light Source (ALS) at Lawrence Berkeley National Lab in Berkeley, California at the magnetic spectroscopy beamline 6.3.1. The synchrotron light source accelerates electrons to relativistic speeds before they are moved to a large storage ring [50]. The various beamlines are arranged tangentially to the ring allowing them to extract the x-rays generated by the electrons (Figure 2.9). Measurements were performed in Total Electron Yield (TEY) mode. TEY mode is a technique which measures an electron current generated in the material during the X-ray absorption which is related to both radiative and non-radiative processes. From this generated current the photo-absorption cross section can be determined.

2.5 UV-Vis Spectroscopy

Ultraviolet-visible Spectroscopy (UV-Vis) is a type of absorption spectroscopy that uses light ranging from wavelengths of 200-800 nm to characterize molecules and compounds [51-53]. The absorption bands of the material are indicative of its physical structure and can shift in wavelength and intensity depending on the nature of the molecule and certain external parameters, such as temperature. Absorbance occurs when the energy of the incoming light excites electrons to a higher orbital. Generally, only electrons within the highest occupied molecular orbital (HOMO) are promoted to the lowest unoccupied molecular orbital (LUMO). The Beer-Lambert Law [54, 55] describes the absorbance of a material as

$$A = \varepsilon l c$$

where ε is the absorptivity of the material, l is the optical path length through the material and c is the concentration of the material.

In a typical UV-Vis measurement, the wavelength of light is ramped between a minimum and maximum value, generating a plot of absorbance as a function of wavelength. For many SCO and VT transition metal complexes, both the UV-Vis and XAS spectrums will vary depending on which state the molecule is in, which will be explored in Chapter 3. Temperature dependent UV-Vis spectrometry measurements were performed using a Thermo Fisher Scientific G10S UV-Vis spectrometer equipped with a custom-made sample heater (Figure 2.10).

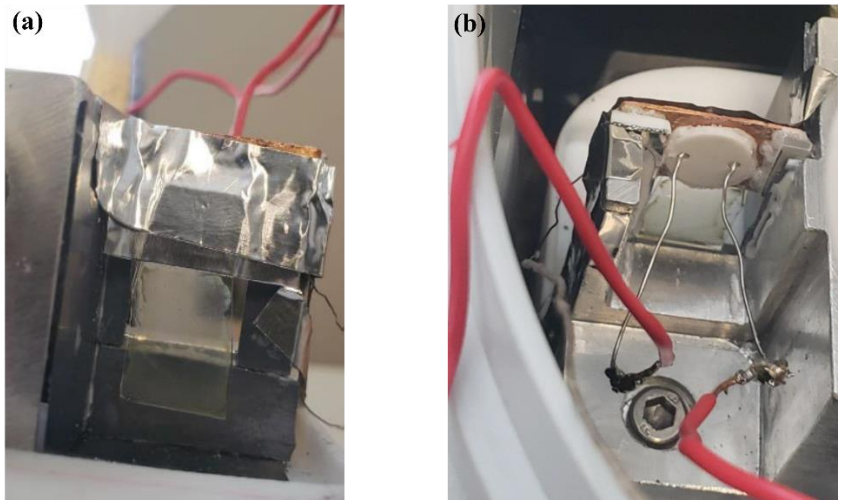

Figure 2.10 (a) A front view of a [Co(sq)(cat)(3-tpp)$_2$] sample mounted onto the custom built UV-Vis sample holder. (b) A rear view of the sample holder, showing the implemented heater.

2.6 Differential Scanning Calorimetry

A Differential Scanning Calorimeter (DSC) is a thermal analysis instrument used to determine the heat flow associated with material transitions as a function of both time and temperature. During an incremental change in temperature a DSC measures the amount of heat either radiated or absorbed by a sample of interest compared to a reference material. In a heat flux DSC, a small metallic pan containing the sample and a typically empty reference pan are placed on a thermoelectric disc inside of a furnace. As the furnace is heated, or cooled, heat flows from the sample and the reference through the thermoelectric disc. Due to the heat capacity, Cp of the material, there should exist a difference in temperature between the sample and reference pans, which is measured through thermocouple wires (Figure 2.11). The heat flow, Q into the sample is given by

$$Q = \frac{\Delta T}{R}$$

Where ΔT is the temperature difference between the sample and reference and R is the resistance of the disc [56].

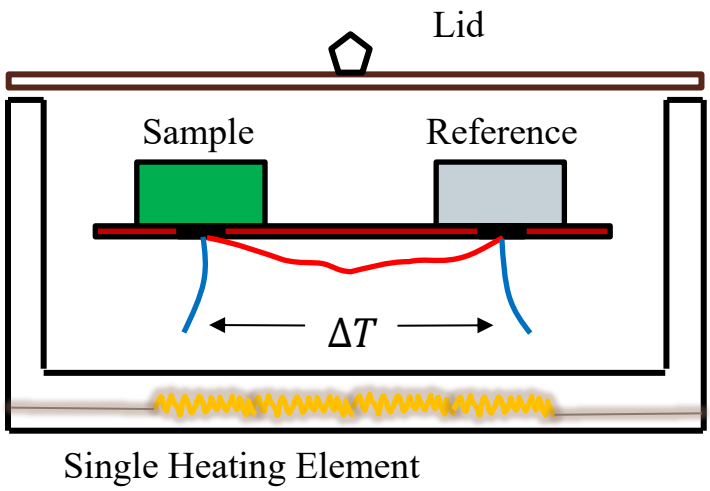

Figure 2.11 The working principle behind a heat-flux Differential Scanning Calorimeter. The heater uniformly heats both the sample and reference crucibles. The heat flow into the sample is determined by the difference in temperature measured by the two blue thermocouple wires.

Calorimeter measurements were performed by Sky Semone in Dr. Gregory Kenning's research lab at the Indiana University of Pennsylvania using a Netzsch – DSC 200 F3 Differential Scanning Calorimeter. The data acquisition software for this model DSC automatically subtracts the baseline measurement from the overall data.

CHAPTER 3. DATA ANALYSIS

3.1 Temperature Dependent XAS of [Co(sq)(cat)(3-tpp)$_2$]

Roughly 300 nm thin films of [Co(sq)(cat)(3-tpp)$_2$] deposited on HOPG were first mounted directly onto the copper sample holder via carbon tape. Next, each sample was painted with a strip of silver paint along the edge to ensure good electrical contact between the sample and the conductive copper holder (Figure 3.1). As mentioned previously, TEY mode is based upon the cascade of primary and secondary electrons at the surface of a sample under test which creates a signal-current through the sample and out through the sample holder. After attaching the samples, the holder was inserted into a degassing chamber where it was held for 24 hours before being placed into the main sample chamber.

Figure 3.1 TEY sample holder with 7 samples attached.

The reported X-ray absorption energies for cobalt are 778.6 eV at the L_3 edge, corresponding to an excitation of a core $2p_{3/2}$ electron and 793.8 eV at the L_2 edge, corresponding to an excitation of a core $2p_{1/2}$ electron. Temperature dependent XAS data of [Co(sq)(cat)(3-tpp)$_2$] deposited on HOPG reveals a slight shift and a splitting of the L_3 edge into absorption peaks

centered near 775.8 eV (t_{2g}) and 777.1 eV (e_g) respectively. Furthermore, the intensity of the absorption peaks change, when increasing the temperature from 300 K to 390 K, with a transition temperature near 370 K (Figure 3.2a). This is likely corresponding to a shift in orbital population due to a change in spin state of the molecule. As the temperature increases, the fraction of molecules in the HS state increases, meaning more electrons are excited into the lower energy t_{2g} orbitals. During the following decreasing cycle from 390 K back to 300 K, the thin film appears to become partially locked, unable to transition back to its original state (Figure 3.2b), with repeated temperature ramping cycles showing no change. This could be due to several factors, most notably the highly photo-active nature observed in many Co VT molecules [56-60]. The exposure to X-rays might cause irreversible changes in the structure of the thin film molecules or trap them in a long-lived metastable state [61-64]. Substrate effects are unlikely, as HOPG reportedly interacts rather modestly with SCO materials [65-67].

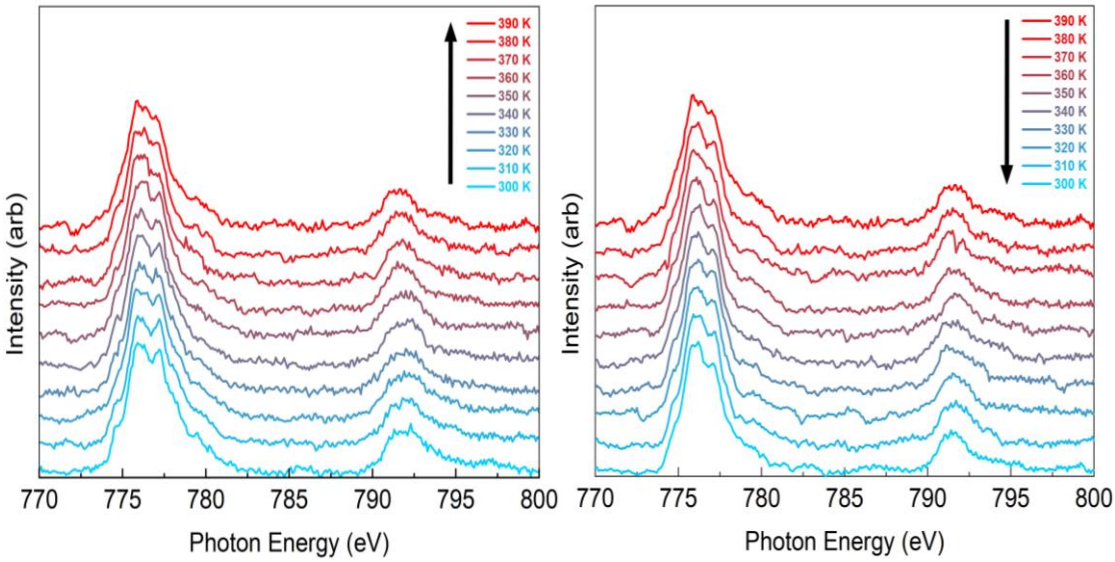

Figure 3.2 Temperature dependent XAS of a thin film of [Co(SQ)(Cat)(3-tpp)$_2$] on a HOPG substrate with (a) an initial increasing temperature cycle (b) and subsequent decreasing temperature cycle. After a L_3-edge shift near 370 K on the initial ramp up, the material becomes locked, unable to transition back.

3.2 Temperature Dependent UV-Vis of [Co(sq)(cat)(3-tpp)$_2$]

A similar transition temperature and locking behavior is observed in temperature dependent UV-Vis data taken for 500 nm of [Co(sq)(cat)(3-tpp)$_2$] deposited on glass substrates. During the initial ramping from 298 K to 400 K, the absorption band centered around 275 nm- which is likely a Ligand-to-Metal Charge-Transfer band (LMCT)- begins to transition at 370 K before reaching its final shape at 400 K (Figure 3.3a), suggesting a change in spin state. Also evident is the decrease in the peak height centered at the d-d transition band at 400 nm. Upon ramping back down from 400 K (Figure 3.3b), no change in the absorbance peaks are observed, signifying that the molecule has apparently become locked in its spin state. Similar to the phenomenon witnessed in the XAS measurements, this locking might be due to the molecule's exposure to UV light.

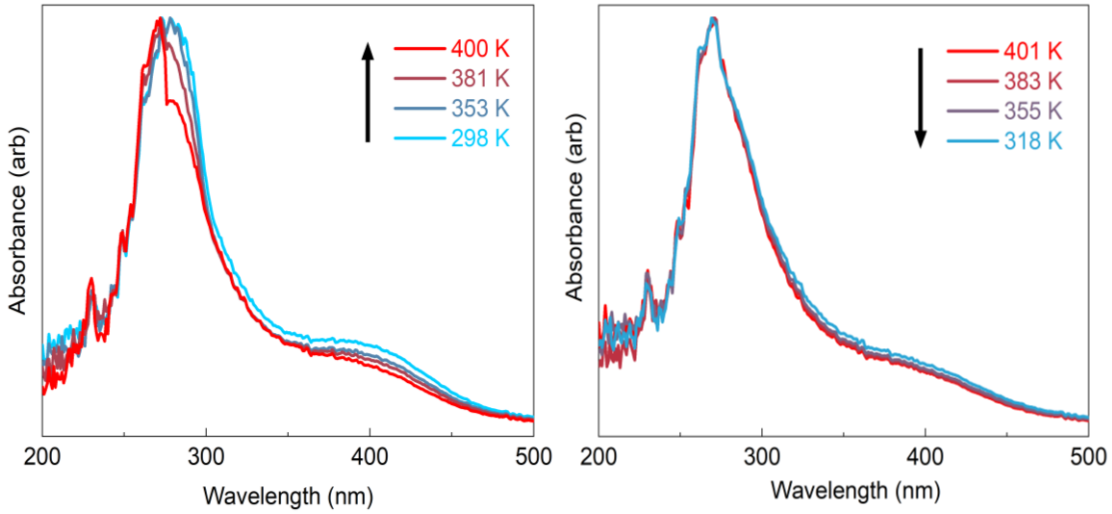

Figure 3.3 Normalized temperature dependent UV-Vis spectra of a thin film of [Co(SQ)(Cat)(3-tpp)$_2$] on a glass substrate with (a) an initial increasing temperature cycle (b) and subsequent decreasing temperature cycle. During the increasing temperature cycle, a clear change in the absorbance spectrum is observed. Upon decreasing the temperature, no change is observed. Intermediate temperatures have been omitted for visual clarity.

Judging from both the XAS and UV-Vis data, thin films of [Co(SQ)(Cat)(3-tpp)$_2$] possess a transition temperature near 370 K. Independent of substrate type, the molecule appears to become locked after an initial spin state transition, which is likely due to the photo-active nature of the molecule.

3.3 Temperature Dependent Transport Properties of [Co(sq)(cat)(3-tpp)$_2$]

For electronic transport measurements, background conductance readings of the IDEs were performed first to ensure an adequately clean surface. A picoammeter reading in the range of 1×10^{-12} Amps designated a suitable substrate. Next, 50uL of a [Co(sq)(cat)(3-tpp)$_2$] molecule + toluene solution was drop cast onto the IDE substrate and allowed to dry while under vacuum. Light and temperature dependent electronic transport measurements were then performed by subjecting the sample to specific temperatures and wavelengths of light while performing sweeping bias loops typically ranging between ±1.4 V. The resulting conductance measurements were not only remarkably high, but also exhibited intricate bias, light and temperature interdependence, particularly near or beyond the same transition temperature of 370 K, as seen both in the XAS and UV-Vis data.

To elaborate more on the general measurement process; beginning first at room temperature, a slow I-V measurement was performed (7 minutes per sweep, 6 seconds per data point, at increments of 0.1 V). The temperature was then slowly increased to the next value and allowed to settle, typically in increments of 10 to 20 K, and with wait times of 10 minutes, before another bias sweep was performed. Once a bias sweep at the maximum temperature was completed, the measurements were repeated while decreasing the temperature. The entire process yielded individual I-V plots as a function of temperature. For clarity, we have omitted presenting the raw data in the form of conductance plots, as they tend to be difficult to interpret visually. Presenting the data as the average conductivity as a function of temperature is more informative.

Figure 3.4a shows the conductivity of **Sample 1** as a function of temperature while under total darkness. The increasing and decreasing temperature cycle showed no change in conductivity, even after many repeated temperature loops, indicating that the molecule was either unable to transition to a HS state, or that it did transition, but the conductivity of the molecule was unaffected. Figure 3.4b show the conductivity of **Sample 2** while illuminated by an incandescent light source. During the first temperature ramping cycle, the conductivity increased by a factor of two near the transition temperature, where it became locked, even after decreasing the temperature and after subsequent temperature-bias ramping. Furthermore, removing the light after many temperature cycles seemed to have no effect once the sample became locked in the higher conductive state, however, this is not entirely conclusive, as the samples may also degrade and lose functionality over time. Figure 3.4c is a plot of raw conductance data illustrating how the conductivity typically

transitions during a temperature-bias sweep while under the effect of incandescent light. In this instance, the sample starts in a lower conductive state, seen in the first 333 K plot. In the process of the bias sweep at 373 K, the conductivity jumps to a higher state near 1.25 V, where it remains during the decreasing temperature cycle.

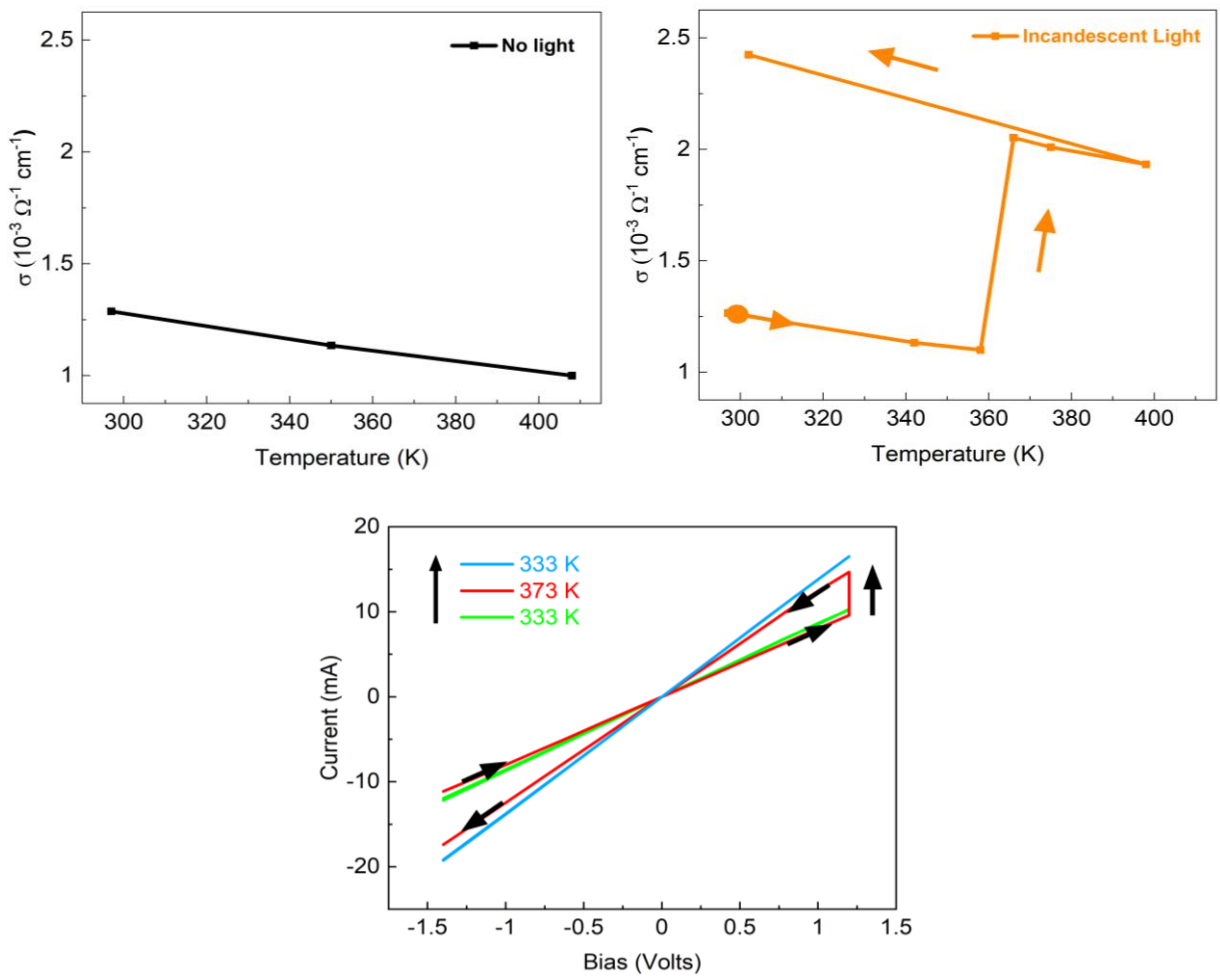

Figure 3.4 Temperature, light and bias dependent conductivity of [Co(SQ)(Cat)(3-tpp)$_2$] thin films on an IDE. (a) The temperature dependent conductivity plot of **Sample 1** while in darkness. (b) The temperature dependent conductivity plot of **Sample 2** while held under incandescent light (c) Raw conductance data of a sample held under incandescent light.

We observed that changes in the conductivity occur more frequently at higher bias magnitudes, although changes are not limited to higher biases. Often, the conductivity is observed to switch back and forth repeatedly during temperature ramping. In Figure 3.5 we see the

conductivity switching between two values while at temperatures near the transition temperature and higher. This indicates a similarity in energy between the low spin and high spin states.

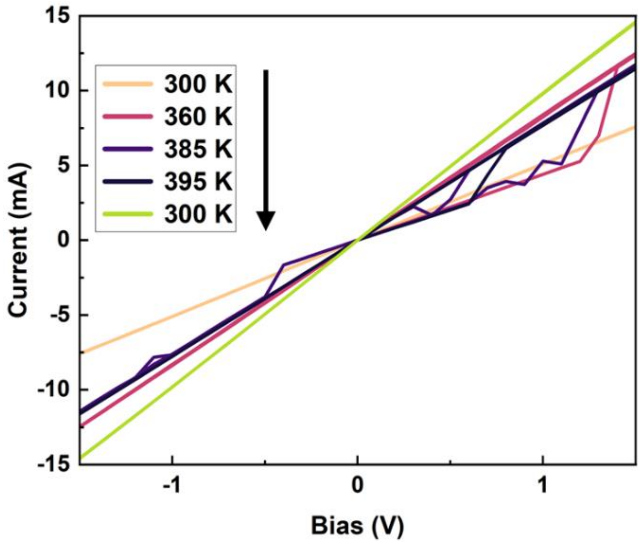

Figure 3.5 IV curve ramping from +/- 2 V showing the "hopping" between conductance values of a sample illuminated by white light while near the transition temperature (some intermediate temperatures have been omitted for clarity).

Sample 3 was first illuminated by a violet wavelength LED during the temperature-bias ramping process (Figure 3.6a). Cycle 1 begins with a conductivity in the bottom range and fully transitions to the middle range upon reaching a temperature of 390 K. Cycle 2 begins where Cycle 1 ends and transitions back down to the lower range. This phenomenon of switching back and forth between two values while under violet LED illumination was observed in multiple samples. The sample's conductivity "switches" at temperatures near 390 K, retaining its value until the temperature is ramped again, after which it "switches" again in the opposite direction. A similar switching behavior in a SCO molecule has been reported previously [68, 69]. Data acquired from multiple samples subject to light wavelengths in the violet range demonstrated that the conductivity could be "toggled" repeatedly. Interestingly, when the light illuminating **Sample 3** was changed to a wavelength in the red region of the visible spectrum, the conductivity stopped transitioning. Cycles 3, 4, 5 were all performed under red light, while Cycles 6, 7, 8 were once again performed under violet light (Figure 3.6b). Cycles 3-6 all follow the lower range and are nearly identical in value to that of Figure 3.4a. With Cycle 7, the conductivity gradually begins to

switch back and forth between both values. By Cycle 8, we return to the same behavior as in the first 2 cycles.

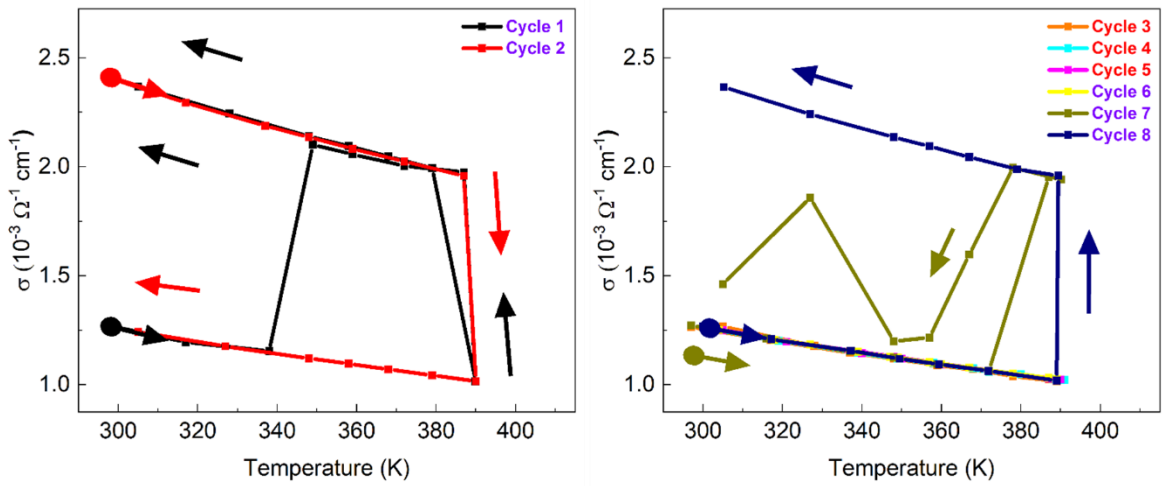

Figure 3.6 LED light, temperature, and bias dependent conductivity of [Co(SQ)(Cat)(3-tpp)$_2$] thin films on an IDE. (a) The temperature dependent conductivity of **Sample 3** while illuminated by a violet wavelength LED for the first 2 cycles. (b) Conductivity plots of Sample 3 for Cycles 3-8. Cycles 3, 4, 5 were illuminated by a red wavelength LED, while Cycles 6, 7, 8 were once again illuminated by a violet LED.

We've eliminated the possibility that this behavior is due to the IDE itself or somehow equipment related. After acquiring data, IDEs have been thoroughly cleaned via sonication, with their background conductance recovered. The experiment was then repeated using the same IDE. We've also utilized two entirely different power supplies and ammeters, yielding the same results.

As mentioned previously, the conductivity of the [Co(sq)(cat)(3-tpp)$_2$] molecule when deposited as a thin film between interdigitated electrodes is remarkably high compared to many other SCO and VT molecules that mostly exhibit insulator-like conductivities [70, 71]. To be a feasible option for a molecular-based electronic device or sensor of some kind, the molecule needs to be reasonably conductive, which makes [Co(sq)(cat)(3-tpp)$_2$] particularly intriguing.

Conductivity values for the molecule were calculated as follows. By considering the dimensions of an individual IDE, with an electrode gap of 5 µm and a total electrode length of 0.98 m and assuming an ideal uniform thin film thickness deposition of 200 nm (the max height of the electrodes), the resistivity of the deposited material can be approximated by the equation

$$\rho = R\frac{A}{L}$$

Where R is the measured resistance, A is the electrode height multiplied by the electrode length, and L is the electrode gap.

After inserting values, a simplified form of the equation can be written

$$\rho = R\frac{(2 \times 10^{-7}\ m) * (0.98\ m)}{5 \times 10^{-6}\ m} \sim 0.04\ Rm$$

with conductivity given by

$$\sigma = \frac{1}{\rho} = 25\ R^{-1}m^{-1}$$

By inserting the values of the slope from the measured I-V plots (Figure 3.4c), which are equivalent to R^{-1}, the conductivity can be calculated.

3.4 Calorimetry Study of [Co(sq)(cat)(3-tpp)$_2$]

As mentioned previously, the mechanism behind the interconversion between LS and HS is an entropy-driven process. This involves both a change in the bond lengths between the transition metal ion and the ligands as well as a change in the density of vibrational states. Heat capacity is a physical property directly related to the molecular degrees of freedom of a material, making calorimetry an excellent experimental tool for probing the nature of the thermally activated valence tautomer interconversion [72-74].

In a thermogram, peaks and valleys correspond to phase changes or chemical reactions occurring in the material. The most common types of transitions can be seen in Figure 3.7. Glass transitions are normally seen in amorphous materials and are due to changes in heat capacity without the occurrence of a phase change.

Looking at the figure and considering water as an example, we would expect to see an exothermic transition if the temperature was ramped down from room temperature to below 0 ºC as the water crystallized into ice, and vice versa. By taking the area under the curve, one could then calculate ΔH, otherwise known in this case as the latent heat of fusion of water.

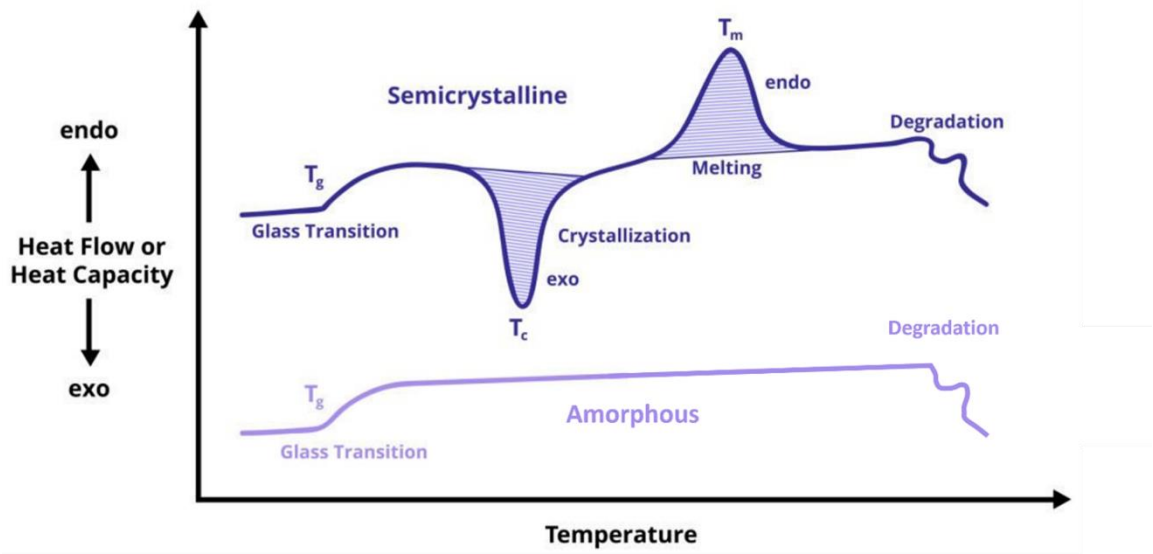

Figure 3.7 Thermogram schematic illustrating the characteristic thermal transitions different materials undergo.

In Figure 3.8. we see two full ramping cycles for a powder sample of [Co(sq)(cat)(3-tpp)$_2$]. In the initial temperature ramping of cycle 1 there is a broad peak centered around the same transition temperature reported earlier (~360 K), which is likely due to a transition of the molecule from LS to HS. On the ramp back down there is a slight dip, again near the transition temperature, indicating that a partial phase change of some kind has occurred. After the first cycle was completed, the second cycle was performed. Here, we see no noticeable transition during the heating cycle. The material exhibits metallic behavior, with a heat capacity that increases linearly with increasing temperature. This too is reminiscent of the electronic transport data, where the material mostly displayed ohmic behavior in between the major transitions of the conductivity. During the cooldown, however, we again see a slight dip near the transition temperature.

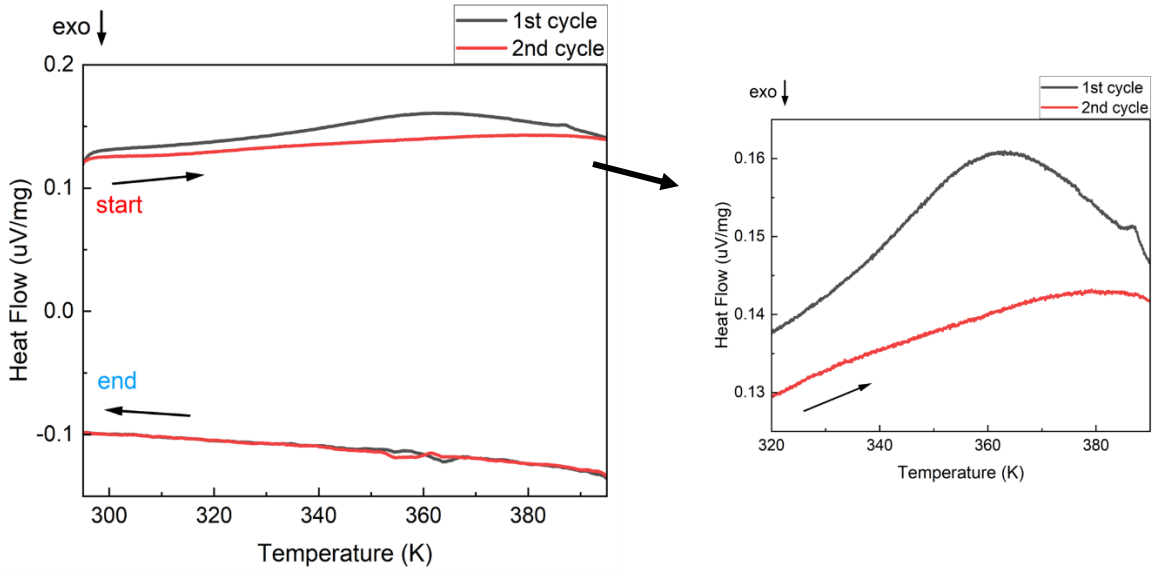

Figure 3.8 Thermogram of two thermal cycles of [Co(sq)(cat)(3-tpp)$_2$] ramped from 300 K-400 K-300 K. The graph on the right shows a zoomed in version of the endothermic peak from the graph on the left.

The broad shape of the endothermic peak is typically indicative of a system with low cooperativity. It can also indicate that the material is diluted with an excess of solvate molecules and uncoordinated Co ions. Comparing this data to a thermogram taken on the same instrument for another, extensively studied SCO molecule, [Fe{$H_2B(pz)_2$}$_2$(bipy)] [75,76], can help to further illustrate (Figure 3.9). [Fe{$H_2B(pz)_2$}$_2$(bipy)] is known to be a highly cooperative material with a reversible thermal spin state transition. Here, we can see as the temperature is decreased towards the transition temperature of the molecule, there is a well-defined phase transition curve. Here, the molecule clearly transitions from HS to LS. When the temperature is ramped back up, we once again see a curve that mirrors the initial one, in the shape of a hysteresis loop. Here, the molecule transitions from LS back to HS.

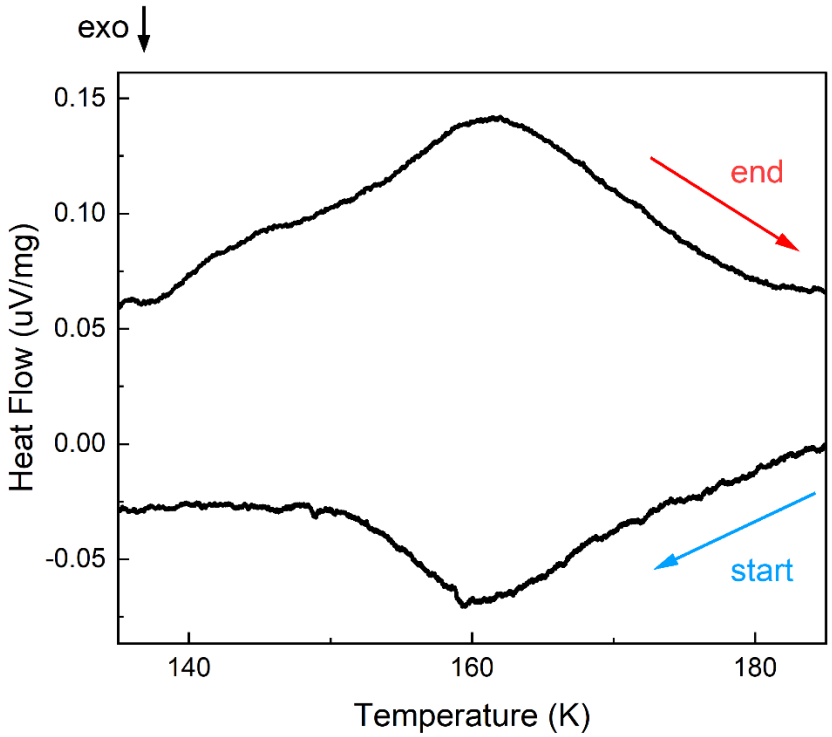

Figure 3.9 Thermogram of the spin crossover molecule [Fe{$H_2B(pz)_2$}$_2$(bipy)].

One thing to note is that DSC measurements are performed in total darkness. While this allows us to observe the effect that temperature alone has on the material, we are unable to observe the combined effect that light and temperature have. In the absence of light, we might simply be unable to witness a complete and potentially reversible phase transition in [Co(sq)(cat)(3-tpp)$_2$] like we see with [Fe{$H_2B(pz)_2$}$_2$(bipy)], which is not known to interact strongly with light.

3.5 Isothermal Spin State Switching of Bilayer PVDF-HFP/[Co(sq)(cat)(3-tpp)$_2$] Thin Films

In a previous study conducted in our lab, an adjacent thin film layer of PVDF-HFP was deposited next to a thin film of the SCO material [Fe{$H_2B(pz)_2$}$_2$(bipy)]. It was discovered that by using an electric field to polarize the ferroelectric PVDF, the spin state of the [Fe{$H_2B(pz)_2$}$_2$(bipy)] layer could be switched isothermally between spin states. To be realistically viable in an electronic device the ability to isothermally switch the spin state of a SCO or VT material is crucial.

Glass substrates were cut and cleaned via sonication in acetone, methanol and isopropyl. 100 nm thin films of gold were then sputtered onto the substrates to serve as a bottom electrode. A solution of 0.05% PVDF-HFP mixed in acetone was prepared by dissolving 40 mg of PVDF-HFP in 100 mL of acetone while heating to 90 ºC. Then approximately 100 uL of the solution was dropped onto the surface of 200 mL beaker filled with de-ionized water. The gold plated substrates were then coated with 25 monolayers (~0.7 nm each) of PVDF-HFP from the beaker via dip coating. The next step was to post-anneal the Au/PVDF-HFP samples at 130 ºC to ensure optimal β-phase crystalline ordering of the PVDF-HFP. Following annealing, ~300 nm of [Co(sq)(cat)(3-tpp)$_2$] was deposited on the substrates. A custom-built poling device with an adjustable top electrode was then used to polarize the ferroelectric PVDF-HFP layer (Figure 3.10).

Figure 3.10 A custom-built polling station with adjustable top electrode, developed by Aaron Mosey, used to switch ferroelectric PVDF-HFP polarity. The bottom Au electrode is attached via a gold wire and connected to the power supply.

The device works by attaching a gold wire to the bottom gold layer of the substrate, which serves as the bottom electrode. The top electrode can be finely adjusted and approached very close to the thin film surface. By using a voltage of +/- 30 V we can generate electric fields between the electrodes in the range of 300 MV/m or more, which is more than sufficient to pole a single domain of PVDF-HFP. Figure 3.11 shows a cross-section of the deposited samples.

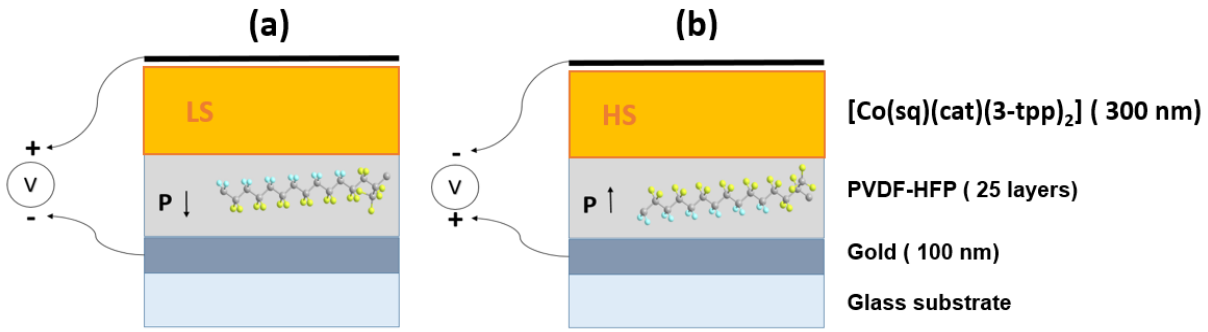

Figure 3.11 Cross-section of bilayer PVDF-HFP/[Co(sq)(cat)(3-tpp)$_2$]. By polarizing the PVDF-HFP toward or away from the [Co(sq)(cat)(3-tpp)$_2$] it can induce a switching between the (a) LS and the (b) HS states.

Interestingly, the spin state appears to be partially switchable isothermally by the polarity of the PVDF-HFP. UV-Vis measurements indicate that there is a coexistence of both the LS and HS states before polarization, evidenced by the broad peak in Figure 3.12. Also of note is the absence of the small peak at 400 nm, which is seen in the temperature dependent UV-Vis data. However, upon closer examination of the data, this peak may have shifted slightly to a lower wavelength. When the PVDF-HFP was polarized away from the [Co(sq)(cat)(3-tpp)$_2$] (down), the peak shifts to the right, reminiscent of the LS spectrum seen previously (Figure 3.3). When the PVDF-HFP is poled up, the peak is much more defined and looks nearly identical to the HS peak measured in the temperature dependent data (Figure 3.3).

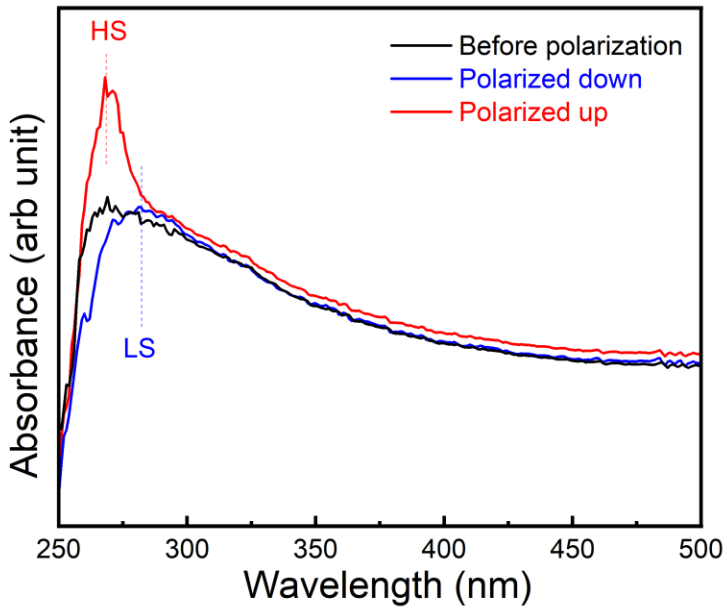

Figure 3.12 Room temperature UV-Vis spectra of bilayer PVDF-HFP (25 layers)/[Co(sq)(cat)(3-tpp)$_2$] (300 nm) samples with PVDF-HFP poled away (down) and toward (up) [Co(sq)(cat)(3-tpp)$_2$].

3.6 The Effect of Doping [Co(sq)(cat)(3-tpp)$_2$] with MXene

In a parallel study, the effect of using the MXene material Ti_3C_2 as a dopant for both [Co(sq)(cat)(3-tpp)$_2$] and [Fe{$H_2B(pz)_2$}$_2$(bipy)] was investigated. This experiment was primarily motivated by the fact that most SCO and VT molecules tend to possess very low conductivities which vastly limits their functionality, with the knowledge from several studies showing that doping can often improve the conductivity of these molecules [77]. Thin films of [Fe{$H_2B(pz)_2$}$_2$(bipy)] in particular exhibit a very low, insulator-like conductivity with low voltage IV data in the picoamp range. However, when doped with Ti_3C_2, we found that the conductivity improved by nearly seven orders of magnitude and the molecule retained its ability to switch from LS and HS (Figure 3.13). Doping consisted of drop casting a 3mg/ml drop of Ti_3C_2 in deionized water onto a thermally evaporated 200 nm thin film of [Fe{$H_2B(pz)_2$}$_2$(bipy)] deposited on a Micrux chip.

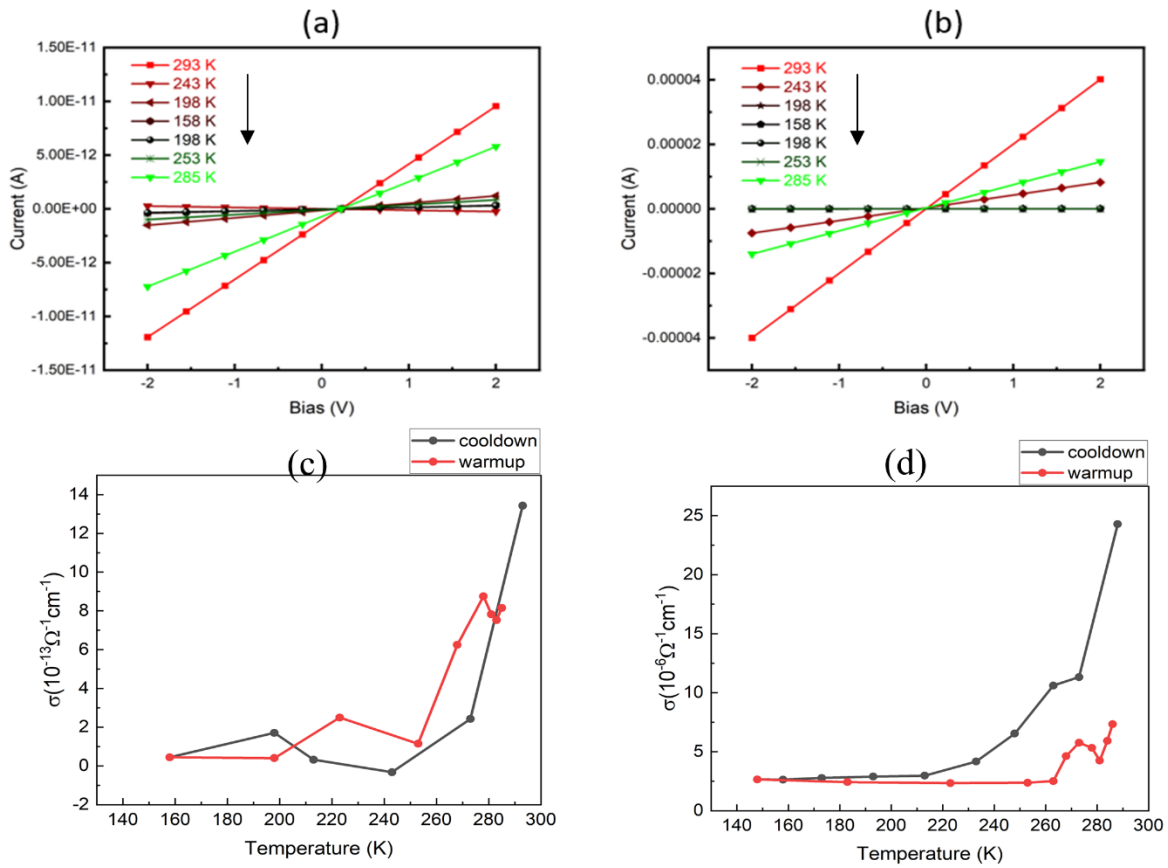

Figure 3.13 Temperature dependent IV plots of [Fe{$H_2B(pz)_2$}$_2$(bipy)] (a) before doping and (b) after doping with Ti_3C_2. Temperature dependent conductivity (c) before doping and (d) after doping.

Another clear indicator that the [Fe{$H_2B(pz)_2$}$_2$(bipy)] thin film retained its switching behavior can be seen in comparing the color of the thin film while above and below the transition temperature of ~160 K. Unlike [Co(sq)(cat)(3-tpp)$_2$] and many other VT molecules, [Fe{$H_2B(pz)_2$}$_2$(bipy)] displays two distinct colors depending on which spin state it inhabits. In Figure 3.14 we see the sample before (a & b) and after (c & d) doping. When at room temperature [Fe{$H_2B(pz)_2$}$_2$(bipy)] displays a light **magenta** color which we see in Figure 3.14a. When subjected to temperatures below 160 K, it transforms into a dark **blue-green** color which is seen in Figure 3.14b. After adding a drop of Ti_3C_2 (the black circular dot in Figure 3.14c) we see the same behavior in c and d as in a and b.

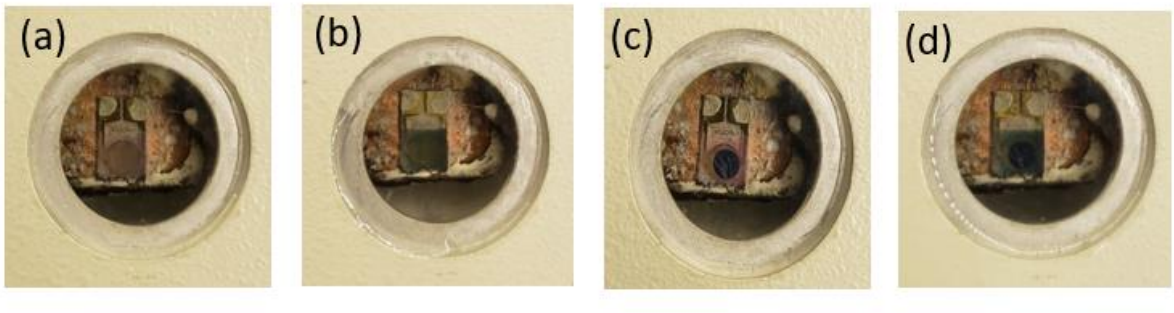

Figure 3.14 Image of 200 [Fe{$H_2B(pz)_2$}$_2$(bipy)] deposited on Micrux sensor without MXene at (a) room temperature and (b) below 160 K, and doped with Ti_3C_2 MXene at (c) room temperature and (d) below 160 K.

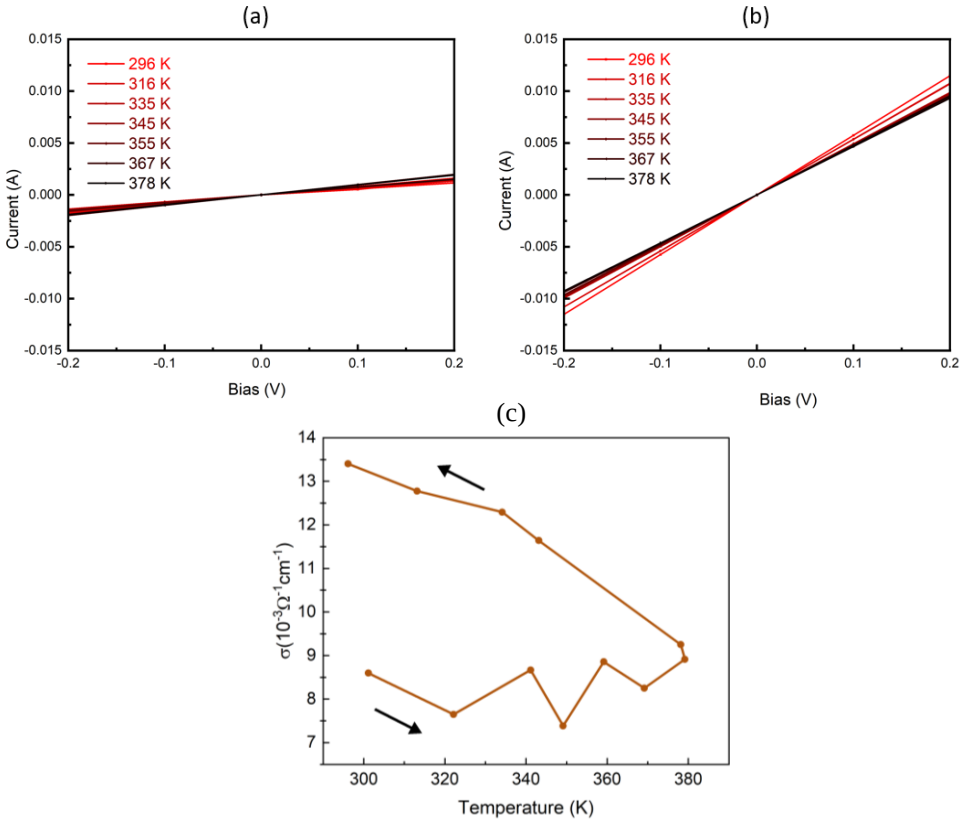

Figure 3.15 Temperature dependent electric transport measurements of 200 nm [Co(sq)(cat)(3-tpp)$_2$] (a) without and (b) with doping with Ti_3C_2 MXene flakes. (c) Conductivity as a function of temperature derived from (b).

As we've seen previously the conductivity of [Co(sq)(cat)(3-tpp)$_2$] stands out and is already quite high in comparison to other SCO and VT molecules, however we still observed an

increase in its conductivity when doped with Ti_3C_2. Figure 3.15 shows IV plots of a Co(sq)(cat)(3-tpp)$_2$] sample before and after doping with Ti_3C_2.

CHAPTER 4. CONCLUSION AND FUTURE WORK

Observed in both the XAS and UV-Vis data, following a temperature induced transition from LS to HS, thin films of the [Co(sq)(cat)(3-tpp)$_2$] molecule become locked in the HS state, unable to switch back. As mentioned previously, this is likely due in part to the highly photo-active nature of cobalt-based valence tautomers. The molecule might experience an irreversible physical change due to light irradiation, particularly via wavelengths in the UV and X-ray range.

Clearly, for [Co(SQ)(Cat)(3-tpp)$_2$], the spin transition is activated both by photon interaction and temperature, and it is also sensitive to the electric field. When the temperature is close to the transition temperature, a photon with a certain high enough energy is required to switch the spin state and the spin state does not appear stable when it is initially switched. After it becomes stable, the spin state does not likely relax back even when the temperature is low enough. This indicates that the low spin state and high spin state likely have relatively comparable energy and the activation energy to switch the spin is reasonably high thus leading to an extensive, long relaxation time. The molecules also appear to have a low degree of cooperativity which might also contribute to the high activation energy.

Additional investigations showed that the implementation of the MXene Ti_3C_2 was seen to improve the conductivity of both [Co(SQ)(Cat)(3-tpp)$_2$] and [Fe{$H_2B(pz)_2$}$_2$(bipy)] and that incorporating a layer of PVDF-HFP adjacent to a layer of [Co(SQ)(Cat)(3-tpp)$_2$] allowed the spin state of the molecule to be switched isothermally by the electric field of the ferroelectric.

Additional experimental techniques to be explored include temperature dependent X-ray diffraction (XRD) [78], and Magneto-Optic Kerr Effect (MOKE) [79] measurements. A recently constructed MOKE, with a built-in sample heater, could provide details about the magnetic properties of the [Co(sq)(cat)(3-tpp)$_2$] molecule as a function of temperature. Diffraction peaks observed in temperature dependent XRD might provide details about variations in the interatomic distances of the molecule. The spin state transition in SCOs and VTs is typically accompanied by changes in volume of the molecules, which would correspond to distinct diffraction peaks at different angles. Initial XRD data indicates that a temperature-dependent shift in the diffraction peak does occur (Figure 3.15). XRD data was taken at the Integrated Nanosystems Development Institute at IUPUI with a monochromatic wavelength of ~1.5406 Å. The d-spacings between

crystal lattice planes for the peaks around 5.85 degrees are roughly 1.50 nm, while the d-spacings for the peaks near 6.1 degrees are roughly 1.45 nm.

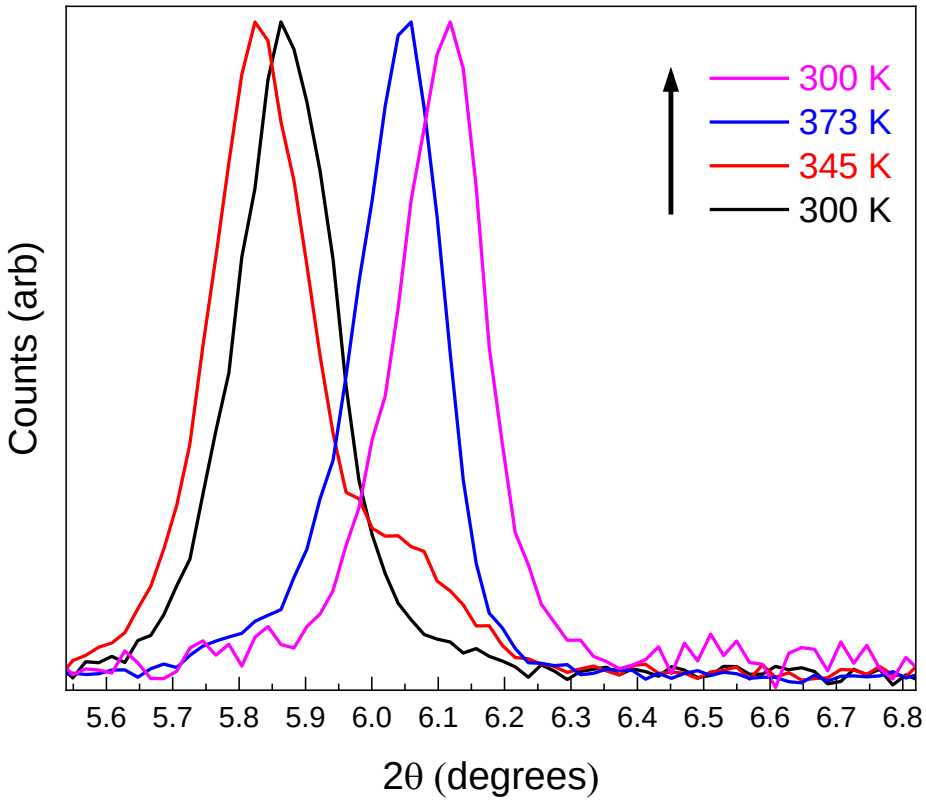

Figure 4.1 Temperature dependent XRD data of [Co(sq)(cat)(3-tpp)$_2$] deposited on Si taken with the help of Brian Wyatt.

REFERENCES

[1] L. Cambi and L. Szegö, *Über Die Magnetische Susceptibilität Der Komplexen Verbindungen*, Ber. Dtsch. Chem. Ges. A/B **64**, 2591 (1931).

[2] L. Cambi and L. Malatesta, *Magnetismus Und Polymorphie Innerer Komplexsalze: Eisensalze Der Dithiocarbamidsäuren*, Ber. Dtsch. Chem. Ges. A/B **70**, 2067 (1937).

[3] W. A. Baker and H. M. Bobonich, *Magnetic Properties of Some High-Spin Complexes of Iron(II)*, Inorg. Chem. **3**, 1184 (1964).

[4] A. Cornia and P. Seneor, *The Molecular Way*, Nature Mater **16**, 505 (2017).

[5] P. Gütlich, Y. Garcia, and H. A. Goodwin, *Spin Crossover Phenomena in Fe(II) Complexes*, Chem. Soc. Rev. **29**, 419 (2000).

[6] P. Gütlich and H. A. Goodwin, *Spin Crossover in Transition Metal Compounds II*, Vol. 234 (Springer Berlin Heidelberg, Berlin, Heidelberg, 2004).

[7] M. Shatruk, H. Phan, B. A. Chrisostomo, and A. Suleimenova, *Symmetry-Breaking Structural Phase Transitions in Spin Crossover Complexes*, Coordination Chemistry Reviews **289–290**, 62 (2015).

[8] D. A. Shultz, *Valence Tautomerism in Dioxolene Complexes of Cobalt*, in *Magnetism: Molecules to Materials II*, edited by J. S. Miller and M. Drillon (Wiley-VCH Verlag GmbH & Co. KGaA, Weinheim, FRG, 2001), pp. 281–306.

[9] R. M. Buchanan and C. G. Pierpont, *Tautomeric Catecholate-Semiquinone Interconversion via Metal-Ligand Electron Transfer. Structural, Spectral, and Magnetic Properties of (3,5-Di-Tert-Butylcatecholato)(3,5-Di-Tert-Butylsemiquinone)(Bipyridyl)Cobalt(III), a Complex Containing Mixed-Valence Organic Ligands*, J. Am. Chem. Soc. **102**, 4951 (1980).

[10] P. Gütlich and A. Dei, *Valence Tautomeric Interconversion in Transition Metal 1,2-Benzoquinone Complexes*, Angew. Chem. Int. Ed. Engl. **36**, 2734 (1997).

[11] T. Tezgerevska, K. G. Alley, and C. Boskovic, *Valence Tautomerism in Metal Complexes: Stimulated and Reversible Intramolecular Electron Transfer between Metal Centers and Organic Ligands*, Coordination Chemistry Reviews **268**, 23 (2014).

[12] E. Evangelio and D. Ruiz-Molina, *Valence Tautomerism: New Challenges for Electroactive Ligands*, Eur J Inorg Chem **2005**, 2957 (2005).

[13] H. Bethe, *Termaufspaltung in Kristallen*, Ann. Phys. **395**, 133 (1929).

[14] R. G. Burns, *Mineralogical Applications of Crystal Field Theory*, 2nd ed (Cambridge University Press, Cambridge [England]; New York, NY, USA, 1993).

[15] C. J. Ballhausen, *Introduction to Ligand Field Theory* (McGraw-Hill, New York, N.Y., 1962).

[16] J. J. Zuckerman, *Some Aspects of Crystal Field Theory (Dunn, Thomas M.; McClure, Donald S.; Pearson, Ralph G.)*, J. Chem. Educ. **43**, 224 (1966).

[17] P. Gütlich, A. B. Gaspar, and Y. Garcia, *Spin State Switching in Iron Coordination Compounds*, Beilstein J. Org. Chem. **9**, 342 (2013).

[18] M. Poulsen and S. Ducharme, *Why Ferroelectric Polyvinylidene Fluoride Is Special*, IEEE Trans. Dielect. Electr. Insul. **17**, 1028 (2010).

[19] Liu, F., Hashim, N. A., Liu, Y., Abed, M. R. M., & Li, K. (2011). Progress in the production and modification of PVDF membranes. *Journal of Membrane Science*, *375*(1-2), 1–27.

[20] Ruan, L., Yao, X., Chang, Y., Zhou, L., Qin, G., & Zhang, X. (2018). Properties and applications of the β phase poly(vinylidene fluoride). *Polymers*, *10*(3), 228.

[21] Tashiro, K. (1995). Crystal structure and phase transition of PVDF and related copolymers. *Ferroelectric Polymers*, 79–198.

[22] Martins, P., Lopes, A. C., & Lanceros-Mendez, S. (2014). Electroactive phases of poly(vinylidene fluoride): Determination, processing and applications. *Progress in Polymer Science*, *39*(4), 683–706.

[23] Jayasuriya, A. C., Schirokauer, A., & Scheinbeim, J. I. (2001). Crystal-structure dependence of electroactive properties in differently prepared poly(vinylidene fluoride/hexafluoropropylene) copolymer films. *Journal of Polymer Science Part B: Polymer Physics*, *39*(22), 2793–2799.

[24] Salimi, A., & Yousefi, A. A. (2003). Analysis method. *Polymer Testing*, *22*(6), 699–704.

[25] Rajesh, P. S., Bodkhe, S., Kamle, S., & Verma, V. (2014). Enhancing beta-phase in PVDF through physicochemical modification of cellulose. *Electronic Materials Letters*, *10*(1), 315–319.

[26] Anasori, B., Lukatskaya, M. R., & Gogotsi, Y. (2017). 2d Metal carbides and nitrides (mxenes) for Energy Storage. *Nature Reviews Materials*, *2*(2).

[27] Lei, J.-C., Zhang, X., & Zhou, Z. (2015). Recent advances in mxene: Preparation, properties, and applications. *Frontiers of Physics*, *10*(3), 276–286.

[28] Zhan, X., Si, C., Zhou, J., & Sun, Z. (2020). MXene and mxene-based composites: Synthesis, properties and environment-related applications. *Nanoscale Horizons*, *5*(2), 235–258.

[29] Rasheed, P. A., Pandey, R. P., Banat, F., & Hasan, S. W. (2022). Recent advances in Niobium Mxenes: Synthesis, properties, and emerging applications. *Matter*, *5*(2), 546–572.

[30] Lim, K. R., Shekhirev, M., Wyatt, B. C., Anasori, B., Gogotsi, Y., & Seh, Z. W. (2022). Fundamentals of mxene synthesis. *Nature Synthesis*, *1*(8), 601–614.

[31] Li, X., Wang, C., Cao, Y., & Wang, G. (2018). Functional mxene materials: Progress of their applications. *Chemistry - An Asian Journal*, *13*(19), 2742–2757.

[32] Zhou, C., Zhao, X., Xiong, Y., Tang, Y., Ma, X., Tao, Q., Sun, C., & Xu, W. (2022). A review of etching methods of mxene and applications of MXene conductive hydrogels. *European Polymer Journal*, *167*, 111063.

[33] Verger, L., Natu, V., Carey, M., & Barsoum, M. W. (2019). Mxenes: An introduction of their synthesis, select properties, and applications. *Trends in Chemistry*, *1*(7), 656–669.

[34] Zhan, X., Si, C., Zhou, J., & Sun, Z. (2020). MXene and mxene-based composites: Synthesis, properties and environment-related applications. *Nanoscale Horizons*, *5*(2), 235–258.

[35] Zhang, S., Huang, P., Wang, J., Zhuang, Z., Zhang, Z., & Han, W.-Q. (2020). Fast and universal solution-phase flocculation strategy for scalable synthesis of various few-layered mxene powders. *The Journal of Physical Chemistry Letters*, *11*(4), 1247–1254.

[36] Alhabeb, M., Maleski, K., Anasori, B., Lelyukh, P., Clark, L., Sin, S., & Gogotsi, Y. (2017). Guidelines for synthesis and processing of two-dimensional titanium carbide (Ti_3C_2T*x* mxene). *Chemistry of Materials*, *29*(18), 7633–7644.

[37] Kumar, J. A., Prakash, P., Krithiga, T., Amarnath, D. J., Premkumar, J., Rajamohan, N., Vasseghian, Y., Saravanan, P., & Rajasimman, M. (2022). Methods of synthesis, characteristics, and environmental applications of mxene: A comprehensive review. *Chemosphere*, *286*, 131607.

[38] Zhang, Y.-Z., El-Demellawi, J. K., Jiang, Q., Ge, G., Liang, H., Lee, K., Dong, X., & Alshareef, H. N. (2020). MXene Hydrogels: Fundamentals and applications. *Chemical Society Reviews*, *49*(20), 7229–7251.

[39] Jatoi, A. S., Mubarak, N. M., Hashmi, Z., Solangi, N. H., Karri, R. R., Tan, Y. H., Mazari, S. A., Koduru, J. R., & Alfantazi, A. (2023). New insights into mxene applications for sustainable environmental remediation. *Chemosphere*, *313*, 137497.

[40] Wu, X., Ma, P., Sun, Y., Du, F., Song, D., & Xu, G. (2021). Application of mxene in electrochemical sensors: A Review. *Electroanalysis*, *33*(8), 1827–1851.

[41] Yu, L., Liu, B., Wang, Y., Yu, F., & Ma, J. (2021). Recent progress on mxene-derived material and its' application in Energy and Environment. *Journal of Power Sources*, *490*, 229250.

[42] Mishra, Esha, Ekanayaka, Thilini K., Panagiotakopoulos, Theodoros, Le, Duy, Rahman, Talat S., Wang, Ping, McElveen, Kayleigh A., Phillips, Jared P., Zaid Zaz, M., Yazdani, Saeed, N'Diaye, Alpha T., Lai, Rebecca Y., Streubel, Robert, Cheng, Ruihua, Shatruk, Michael, & Dowben, Peter A. Electronic structure of cobalt valence tautomeric molecules in different environments. United Kingdom.

[43] A. Kaliyaraj Selva Kumar, Y. Zhang, D. Li, and R. G. Compton, *A Mini-Review: How Reliable Is the Drop Casting Technique?*, Electrochemistry Communications **121**, 106867 (2020).

[44] J. P. Phillips, S. Yazdani, W. Highland, and R. Cheng, *A High Sensitivity Custom-Built Vibrating Sample Magnetometer*, Magnetochemistry **8**, 84 (2022).

[45] A. Zieba and S. Foner, *Detection Coil, Sensitivity Function, and Sample Geometry Effects for Vibrating Sample Magnetometers*, Review of Scientific Instruments **53**, 1344 (1982).

[46] E. E. Bragg and M. S. Seehra, *Analysis of Induced EMF in Vibrating-Sample Magnetometers*, J. Phys. E: Sci. Instrum. **9**, 216 (1976).

[47] J. Mallinson, *Magnetometer Coils and Reciprocity*, Journal of Applied Physics **37**, 2514 (1966).

[48] *The Magnetization of Pure Iron and Nickel*, Proc. R. Soc. Lond. A **321**, 477 (1971).

[49] F. Hippert, E. Geissler, J. L. Hodeau, E. Lelièvre-Berna, and J.-R. Regnard, editors , *Neutron and X-Ray Spectroscopy* (Springer Netherlands, Dordrecht, 2006).

[50] P. Willmott, *An Introduction to Synchrotron Radiation: Techniques and Applications* (John Wiley, Chichester, West Sussex, UK, 2011).

[51] T. Konevskikh, A. Ponossov, R. Blümel, R. Lukacs, and A. Kohler, *Fringes in FTIR Spectroscopy Revisited: Understanding and Modelling Fringes in Infrared Spectroscopy of Thin Films*, Analyst **140**, 3969 (2015).

[52] H. Naggert, A. Bannwarth, S. Chemnitz, T. von Hofe, E. Quandt, and F. Tuczek, *First Observation of Light-Induced Spin Change in Vacuum Deposited Thin Films of Iron Spin Crossover Complexes*, Dalton Trans. **40**, 6364 (2011).

[53] M. A. Dubinskii and P. Misra, *Ultraviolet Spectroscopy and UV Lasers* (Marcel Dekker, New York, 2002).

[54] J. D. Ingle and S. R. Crouch, *Spectrochemical Analysis* (Prentice Hall, Englewood Cliffs, N.J, 1988).

[55] T. G. Mayerhöfer, S. Pahlow, and J. Popp, *The Bouguer-Beer-Lambert Law: Shining Light on the Obscure*, ChemPhysChem **21**, 2025 (2020).

[56] Gill P, Moghadam TT, Ranjbar B. *Differential scanning calorimetry techniques: applications in biology and nanoscience*. J Biomol Tech. 2010 Dec;21(4):167-93.

[57] D. N. Hendrickson and C. G. Pierpont, *Valence Tautomeric Transition Metal Complexes*, in *Spin Crossover in Transition Metal Compounds II*, Vol. 234 (Springer Berlin Heidelberg, Berlin, Heidelberg, 2004), pp. 63–95.

[58] R. D. Schmidt, D. A. Shultz, and J. D. Martin, *Magnetic Bistability in a Cobalt Bis(Dioxolene) Complex: Long-Lived Photoinduced Valence Tautomerism*, Inorg. Chem. **49**, 3162 (2010).

[59] T. K. Ekanayaka et al., *Evidence of Dynamical Effects and Critical Field in a Cobalt Spin Crossover Complex*, Chem. Commun. **58**, 661 (2022).

[60] T. M. Francisco, W. J. Gee, H. J. Shepherd, M. R. Warren, D. A. Shultz, P. R. Raithby, and C. B. Pinheiro, *Hard X-Ray-Induced Valence Tautomeric Interconversion in Cobalt-* o *-Dioxolene Complexes*, J. Phys. Chem. Lett. **8**, 4774 (2017).

[61] R. D. Schmidt, D. A. Shultz, J. D. Martin, and P. D. Boyle, *Goldilocks Effect in Magnetic Bistability: Remote Substituent Modulation and Lattice Control of Photoinduced Valence Tautomerism and Light-Induced Thermal Hysteresis*, J. Am. Chem. Soc. **132**, 6261 (2010).

[62] D. M. Adams, B. Li, J. D. Simon, and D. N. Hendrickson, *Photoinduced Valence Tautomerism in Cobalt Complexes Containing Semiquinone Anion as Ligand: Dynamics of the High-Spin[CoII(3,5-Dtbsq)2] to Low-Spin[CoIII(3,5-Dtbsq)(3,5-Dtbcat)] Interconversion*, Angew. Chem. Int. Ed. Engl. **34**, 1481 (1995).

[63] O. Sato, S. Hayami, Z. Gu, K. Seki, R. Nakajima, and A. Fujishima, *Photo-Induced Long-Lived Intramolecular Electron Transfer in a Co Valence Tautomeric Complex*, Chem. Lett. **30**, 874 (2001).

[64] G. Poneti, M. Mannini, L. Sorace, P. Sainctavit, M.-A. Arrio, A. Rogalev, F. Wilhelm, and A. Dei, *X-Ray Absorption Spectroscopy as a Probe of Photo- and Thermally Induced Valence Tautomeric Transition in a 1:1 Cobalt-Dioxolene Complex*, ChemPhysChem **10**, 2090 (2009).

[65] J. Dai, S. Kanegawa, Z. Li, S. Kang, and O. Sato, *A Switchable Complex Ligand Exhibiting Photoinduced Valence Tautomerism*, Eur. J. Inorg. Chem. **2013**, 4150 (2013).

[66] L. Kipgen, M. Bernien, F. Nickel, H. Naggert, A. J. Britton, L. M. Arruda, E. Schierle, E. Weschke, F. Tuczek, and W. Kuch, *Soft-x-Ray-Induced Spin-State Switching of an Adsorbed Fe(II) Spin-Crossover Complex*, J. Phys.: Condens. Matter **29**, 394003 (2017).

[67] L. Kipgen et al., *Evolution of Cooperativity in the Spin Transition of an Iron(II) Complex on a Graphite Surface*, Nat Commun **9**, 2984 (2018).

[68] M. Bernien et al., *Highly Efficient Thermal and Light-Induced Spin-State Switching of an Fe(II) Complex in Direct Contact with a Solid Surface*, ACS Nano **9**, 8960 (2015).

[69] F. Prins, M. Monrabal-Capilla, E. A. Osorio, E. Coronado, and H. S. J. van der Zant, *Room-Temperature Electrical Addressing of a Bistable Spin-Crossover Molecular System*, Adv. Mater. **23**, 1545 (2011).

[70] C. Etrillard, V. Faramarzi, J.-F. Dayen, J.-F. Letard, and B. Doudin, *Photoconduction in [Fe(Htrz)2(Trz)](BF4)·H2O Nanocrystals*, Chem. Commun. **47**, 9663 (2011).

[71] A. Rotaru, I. A. Gural'skiy, G. Molnár, L. Salmon, P. Demont, and A. Bousseksou, *Spin State Dependence of Electrical Conductivity of Spin Crossover Materials*, Chem. Commun. **48**, 4163 (2012).

[72] Q. Zheng, Y. Zhang, M. Montazerian, O. Gulbiten, J. C. Mauro, E. D. Zanotto, and Y. Yue, *Understanding Glass through Differential Scanning Calorimetry*, Chem. Rev. **119**, 7848 (2019).

[73] M. Sorai, *Heat Capacity Studies of Spin Crossover Systems*, in *Spin Crossover in Transition Metal Compounds III*, Vol. 235 (Springer-Verlag, Berlin/Heidelberg, 2004), pp. 153–170.

[74] A. Lannes et al., *Room Temperature Magnetic Switchability Assisted by Hysteretic Valence Tautomerism in a Layered Two-Dimensional Manganese-Radical Coordination Framework*, J. Am. Chem. Soc. **138**, 16493 (2016).

[75] A. Mosey, *Voltage Controlled Non-Volatile Spin State and Conductance Switching of a Molecular Thin Film Heterostructure*, (2021).

[76] S. Yazdani, *Study of the Spin Crossover Molecular Thin Films and Magnetic Multilayered Thin Films*, (2023).

[77] Gavara-Edo, M., Córdoba, R., Valverde-Muñoz, F. J., Herrero-Martín, J., Real, J. A., & Coronado, E. (2022). Electrical sensing of the thermal and light-induced spin transition in robust contactless spin-crossover/graphene hybrid devices. *Advanced Materials*, *34*(33), 2202551.

[78] A. L. Ryland, *X-Ray Diffraction*, J. Chem. Educ. **35**, 80 (1958).

[79] K. Sato and T. Ishibashi, *Fundamentals of Magneto-Optical Spectroscopy*, Front. Phys. **10**, 946515 (2022).